Available online at www.sciencedirect.com
ScienceDirect
Comput. Methods Appl. Mech. Engrg. 352 (2019) 369–388
Computer methods in applied mechanics and engineering
www.elsevier.com/locate/cma

The interplay of biochemical and biomechanical degeneration in Alzheimer's disease

A. Schäfer[a], J. Weickenmeier[b], E. Kuhl[a,*]

[a] Department of Mechanical Engineering, Stanford University, Stanford, CA 94305, USA
[b] Department of Mechanical Engineering, Stevens Institute of Technology, Hoboken, NJ 07030, USA

Received 9 November 2018; received in revised form 20 March 2019; accepted 24 April 2019
Available online 13 May 2019

Highlights

- A pronounced decrease in brain volume is a classical hallmark of Alzheimer's disease.
- The patterns of shrinkage are closely related to the distribution of misfolded tau protein.
- We propose a multiphysics model that couples the spreading of misfolded tau to volume loss.
- Our simulations reveal that misfolded protein accelerates natural shrinkage by a factor 3 to 5.
- Volume loss of 3–4%/year accurately predicts atrophy in Alzheimer's disease.
- Regions near the hippocampus are most affected by biochemically induced brain tissue loss.

Abstract

Alzheimer's disease is an irreversible neurodegenerative disorder that manifests itself in the progressive aggregation of misfolded tau protein, neuronal death, and cerebral atrophy. A reliable diagnosis of these changes in the brain is challenging because they typically precede the clinical symptoms of Alzheimer's disease by at least one, if not two, decades. Volumetric magnetic resonance imaging holds promise as a non-invasive biomarker for disease onset and progression by quantifying cerebral atrophy in time and space. Recent studies suggest that the patterns of brain atrophy are closely correlated with the regional distribution of misfolded tau protein; yet, to date, there is no compelling computational model to simulate the interaction of misfolded protein spreading and tissue atrophy. Here we establish a multiphysics model that couples misfolded protein spreading and tissue atrophy to explore the spatio-temporal interplay of biochemical and biomechanical degeneration in Alzheimer's disease. We discretize the coupled bio-chemo-mechanical problem using a nonlinear finite element approach with the misfolded protein concentration and the tissue deformation as primary unknowns. In a systematic parameter study, we probe the role of the individual model parameters and compare our results against cerebral atrophy curves of patients with early onset Alzheimer's disease. A critical link between biochemical and biomechanical degeneration is the atrophy rate, which reflects both natural aging-induced atrophy and accelerated misfolding-induced atrophy. Our simulations reveal that misfolding accelerates natural atrophy by a factor of three to five, and that regions near the hippocampus are most affected by brain tissue loss. Our quantitative model could help improve diagnostic tools, advance early detection, and, ultimately, enable early interventions to delay the onset of cognitive decline in familial or sporadic Alzheimer's disease.

* Corresponding author.
E-mail address: ekuhl@stanford.edu (E. Kuhl).

https://doi.org/10.1016/j.cma.2019.04.028
0045-7825/

Keywords: Fisher–Kolmogorov equation; Finite element analysis; Neuromechanics; Alzheimer's disease

1. Motivation

Alzheimer's disease is an ultimately fatal, neurodegenerative disease affecting more and more people worldwide. In the United States, 10 percent of people age 65 or older are living with Alzheimer's dementia today [1]. The increasing life expectancy makes Alzheimer's disease a growing public health problem [2]. As of today, a reliable diagnosis of Alzheimer's disease is only possible at a late disease stage when interventions have little effect [3]. To develop new diagnostic tools and treatments, it is crucial to find answers to the many open questions regarding the pathogenic cascade of Alzheimer's disease.

Histological evidence suggests that the progression of Alzheimer's disease is related to the spreading of misfolded protein aggregates in the brain [4]. Large assemblies of pathological amyloid-β and tau protein have been found in the form of senile plaques and neurofibrillary tangles in the brains of Alzheimer's patients. These postmortem analyses reveal a stereotypical pattern of protein aggregate propagation [5]. While amyloid-β plaques start to accumulate in the neocortex before spreading into the allo- and subcortex, tau-inclusions first appear in the entorhinal cortex and locus coeruleus and then advance to interconnected cortical areas [4,6]. When taking into account the neuronal connectome of the brain, it becomes clear that axonal transport must play an important role in the spread of misfolded proteins [7]. To this day, the pathways by which pathological protein conformations of amyloid-β and tau develop, grow and spread, are not entirely understood [8]. However, recent findings suggest that the spatio-temporal spreading of neurodegeneration shares many of its key properties with the biology of prion diseases [7,9]. In these infectious diseases, corruptive seeds in the form of misfolded proteins initiate a chain reaction, causing healthy proteins to misfold and grow [10]. While it is difficult to quantify the underlying transport mechanisms in vivo, we can replicate the key features of protein propagation in various neurodegenerative disorders using a nonlinear diffusion model based on the Fisher–Kolmogorov equation [11]. This proposal of a simple physics-based model for neurodegeneration is one of the first attempts to find quantitative explanations for the characteristic observations in Alzheimer's disease [12].

Where proteopathic inclusions of amyloid-β and tau accumulate, they disrupt healthy tissue function and ultimately lead to cell death manifesting in tissue atrophy [13]. Especially the sequential pattern of tauopathy seems to align with the topographic progression of brain atrophy observed in longitudinal magnetic resonance imaging studies [14,15]. Brain volume loss is first observed in the hippocampal regions of the temporal lobes, subsequently affects the frontal lobe and the occipital lobe, and only in late disease stages occurs in the motor and sensory cortex [15]. While the presence and propagation of proteopathic lesions can, to this date, only be reliably quantified postmortem, local changes in brain volume can easily be assessed with conventional imaging methods non-invasively in vivo [16–18].

Fig. 1 illustrates the progressive cerebral atrophy in twelve patients with early-onset Alzheimer's disease recorded during a longitudinal magnetic resonance imaging study [17]. The brain volume is normalized by the intracranial volume and displayed over a time period of 13 years. Year zero represents the time point of clinically diagnosed cognitive impairment defined as an MMSE score of 23 [17]. The solid and dashed red curves represent a second order polynomial fit to the data points and its 95% confidence interval. For comparison, the dashed gray line shows the baseline atrophy in healthy elderly adults [19]. Quantitatively modeling the accelerated tissue atrophy in Alzheimer's disease, induced by misfolded protein, is the objective of this study.

A computational model that relates the spatio-temporal evolution of brain atrophy in Alzheimer's disease to the underlying biological mechanisms that precede the clinical symptoms could provide insight into the ways in which both processes affect each other. A few atrophy models have been proposed in the literature [20–22]; however, these models typically disregard the anisotropy of the tissue, the regional variation of atrophy rates, and the disease-specific pattern in which volume loss occurs. Here we build on our previous prototype model [11] and propose a simple approach to study the interplay of misfolded protein propagation and regional tissue atrophy using a multiphysics finite element analysis. Our model combines a biochemical anisotropic reaction–diffusion model to predict the time-dependent local concentration of misfolded tau protein [12] with a biomechanical finite deformation shrinking model to predict the concentration-dependent regional tissue atrophy [23]. Specifically, we introduce a new constitutive function for tissue atrophy that depends explicitly on the misfolded protein concentration, we analyze

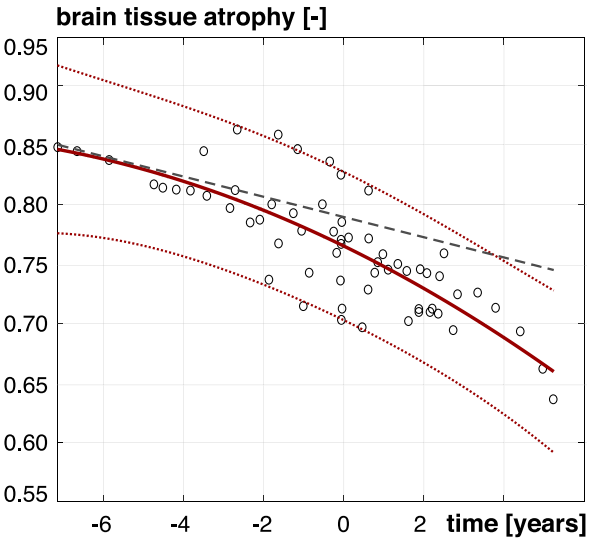

Fig. 1. Progressive brain atrophy in twelve patients with early-onset Alzheimer's disease from a longitudinal magnetic resonance imaging study [17] compared to baseline atrophy in healthy elderly adults [19]. The brain tissue atrophy is normalized by the intracranial volume and displayed throughout a period of 13 years. The zero time point represents the onset of clinically diagnosed cognitive impairment with an MMSE score of 23. The solid red curve represents a second order polynomial fit to the data points; the dashed red curves represent the 95% confidence interval; the dashed gray line indicates the baseline atrophy in healthy elderly adults.

the nature of coupling between biochemical protein misfolding and biomechanical atrophy, we perform a systematic sensitivity analysis of all atrophy-related model parameters, and calibrate our model to atrophy recordings of patients with early-onset Alzheimer's disease. In Section 2, we introduce the governing equations of the coupled protein spreading and tissue atrophy problems and discuss the nature of coupling. In Section 3, we propose a computational model to solve the protein spreading and tissue atrophy problems using a multiphysics finite element approach and show how we can implement a discrete version of the governing equations, either in a stand-alone approach or within existing nonlinear finite element solvers. In Section 4, we prototype our approach using two-dimensional models of the brain that we created from magnetic resonance imaging and tractography data. We perform a systematic sensitivity analysis to study the influence of our model parameters on the spatio-temporal evolution of atrophy and compare our results to the tissue atrophy curves in early onset Alzheimer's disease [17] from Fig. 1. Finally, we discuss our results and provide an outlook towards potential future applications of our model.

2. Continuum modeling of protein spreading and tissue atrophy

Kinematics. We characterize the kinematics of the shrinking brain by the mapping $\boldsymbol{\varphi}$ from the initial configuration $\mathcal{B}_0$ to the current configuration $\mathcal{B}_t$ at time t. We adopt the conventional notation, $\boldsymbol{x} = \boldsymbol{\varphi}(\boldsymbol{X}, t)$, where $\boldsymbol{x} \in \mathcal{B}_t$ denotes spatial coordinates, $\boldsymbol{X} \in \mathcal{B}_0$ material coordinates, $t \in \mathbb{R}_+$ time. The deformation gradient, $\boldsymbol{F}(\boldsymbol{X}, t) = \nabla_{\boldsymbol{X}} \boldsymbol{\varphi}(\boldsymbol{X}, t)$, characterizes local deformations and its determinant, $J = \det(\boldsymbol{F})$, measures the local volume change. To model brain atrophy, we adopt the classical multiplicative decomposition of the deformation gradient, $\boldsymbol{F} = \nabla \boldsymbol{\varphi}$, into an elastic part $\boldsymbol{F}^{\mathrm{e}}$ and an atrophy part $\boldsymbol{F}^{\mathrm{a}}$,

$$\boldsymbol{F} = \nabla \boldsymbol{\varphi} = \boldsymbol{F}^{\mathrm{e}} \cdot \boldsymbol{F}^{\mathrm{a}} \quad \text{and} \quad J = \det(\boldsymbol{F}) = J^{\mathrm{e}} J^{\mathrm{a}}. \tag{1}$$

This multiplicative decomposition carries over to the Jacobian J, where $J^{\mathrm{e}} = \det(\boldsymbol{F}^{\mathrm{e}})$ is the elastic volume change and $J^{\mathrm{a}} = \det(\boldsymbol{F}^{\mathrm{a}})$ is the volume loss by tissue atrophy. The elastic part of the deformation $\boldsymbol{F}^{\mathrm{e}}$ contributes to the elastic strain energy and is fully reversible. The atrophy part $\boldsymbol{F}^{\mathrm{a}}$ defines the tissue loss caused by atrophy and depends on the local concentration of misfolded protein.

Balance equations of protein spreading. We characterize the spreading of misfolded protein c in the initial configuration $\mathcal{B}_0$ through a reaction–diffusion equation with a flux $\boldsymbol{Q}$ and a source F^c,

$$\dot{c} = \mathrm{Div}(\boldsymbol{Q}) + F^c \quad \text{in} \quad \mathcal{B}_0, \tag{2}$$

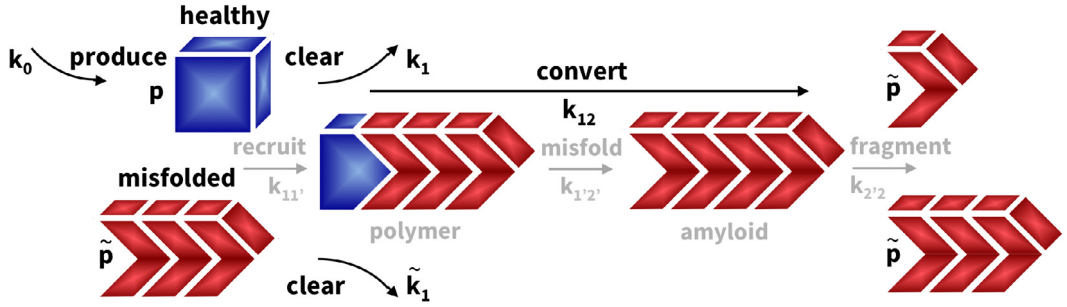

Fig. 2. Kinetics of healthy and misfolded protein. The healthy protein concentration p increases through production k_0 and decreases through clearance k_1 and conversion into misfolded protein k_{12}. The misfolded protein concentration $\tilde{p}$ decreases through clearance $\tilde{k}_1$ and increases through conversion from healthy protein k_{12}. The conversion rate k_{12} collectively represents the recruitment $k_{11'}$ of healthy protein, its misfolding $k_{1'2'}$ on an infectious seed of misfolded protein, and the fragmentation $k_{2'2}$ into new infectious seeds.

where $\dot{c} = \mathrm{d}c/\mathrm{d}t$ denotes the material time derivative of the misfolded protein concentration c. Using Nanson's formula, $\boldsymbol{Q} = J\,\boldsymbol{q}\cdot\boldsymbol{F}^{-\mathrm{t}}$, and the transformation of the source term, $F^c = J\,f^c$, we can rephrase the reaction–diffusion equation (2) in the current configuration $\mathcal{B}_t$,

$$\dot{c} = \mathrm{div}(J\boldsymbol{q}) + f^c \qquad \text{in } \mathcal{B}_t\,. \tag{3}$$

In a continuum sense, the misfolded protein concentration c is an order parameter that varies between $0 \le c \le 1$ and characterizes the degree of misfolding. The nature of coupling between the protein spreading problem and the tissue atrophy problem will depend on whether we choose to introduce constitutive equations for the material or spatial flux $\boldsymbol{Q}$ or $\boldsymbol{q}$ and for the material or spatial source F^c or f^c.

Balance equations of tissue atrophy. We characterize tissue atrophy through the balance of linear momentum in the initial configuration $\mathcal{B}_0$ in terms of the material divergence of the Piola stress $\boldsymbol{P}$ and the external forces $\boldsymbol{F}^\varphi$,

$$\boldsymbol{0} = \mathrm{Div}(\boldsymbol{P}) + \boldsymbol{F}^\varphi \qquad \text{in } \mathcal{B}_0\,. \tag{4}$$

Tissue atrophy usually occurs over months, years, or even decades, which allows us to consider the balance of linear momentum in the quasi-static limit. Similar to the protein spreading problem, we use Nanson's formula, $\boldsymbol{P} = J\boldsymbol{\sigma}\cdot\boldsymbol{F}^{-\mathrm{t}}$, and the relation between the volume forces, $\boldsymbol{F}^\varphi = J\,\boldsymbol{f}^\varphi$, to transform the material version of the mechanical equilibrium equation (4) into its spatial counterpart in the current configuration $\mathcal{B}_t$,

$$\boldsymbol{0} = \mathrm{div}(\boldsymbol{\sigma}) + \boldsymbol{f}^\varphi \qquad \text{in } \mathcal{B}_t\,, \tag{5}$$

where $\boldsymbol{\sigma}$ is the Cauchy stress and $\boldsymbol{f}^\varphi$ is the external force vector. For simplicity, we assume that we can neglect the effect of external forces, $\boldsymbol{F}^\varphi = \boldsymbol{0}$ and $\boldsymbol{f}^\varphi = \boldsymbol{0}$. The material and spatial versions of the tissue atrophy problem (4) and (5) are coupled to the protein spreading problem through the atrophy tensor $\boldsymbol{F}^{\mathrm{a}}$, which we assume to depend on the local misfolded protein concentration c.

Constitutive equations of protein spreading. For the protein spreading problem, we have to define constitutive equations for the material or spatial source, either F^c or f^c, that represents the growth of misfolded protein and for the material or spatial flux, either $\boldsymbol{Q}$ or $\boldsymbol{q}$, that represents the spreading of misfolded protein. Here we introduce both flux and source in the current, spatial configuration. For the source f^c, we adopt our recent protein folding model [12], and assume that the current protein concentration c derives from a kinetic model that balances the total amount of healthy protein p and misfolded tau protein $\tilde{p}$,

$$\frac{\partial p}{\partial t} = k_0 - k_1\,p - k_{12}\,p\,\tilde{p} \qquad \text{and} \qquad \frac{\partial \tilde{p}}{\partial t} = -\tilde{k}_1\,\tilde{p} + k_{12}\,p\,\tilde{p}\,. \tag{6}$$

Fig. 2 illustrates the kinetics of healthy and misfolded protein, where k_0 is the production rate of healthy protein p, k_1 and $\tilde{k}_1$ are the clearance rates of p and $\tilde{p}$, and k_{12} is the conversion rate from the healthy to the misfolded state. In the healthy state, the total amount of healthy protein is simply the ratio between production and clearance, $p_0 = k_0/k_1$. Initially, close to this healthy equilibrium state, the amount of healthy protein is much larger than the

amount of misfolded protein, $p \gg \tilde{p}$, which implies that the rate of change of healthy protein is close to zero, $\partial p/\partial t \approx 0$. With these assumptions Eq. ((6).1) provides an explicit estimate for the amount of healthy protein p,

$$\frac{\partial p}{\partial t} \approx 0 \qquad \text{thus} \qquad p = \frac{k_0}{k_1 + k_{12}\,\tilde{p}}\,. \tag{7}$$

We approximate the amount of healthy protein p using a Taylor series, evaluated at $k_{12}/k_1\,\tilde{p} = 0$, to obtain $p = k_0/k_1\,[\,1 - \tilde{p}\,k_{12}/k_1\,]$, and substitute this back into Eq. ((6).2) to estimate the amount of misfolded protein,

$$\frac{\partial\,\tilde{p}}{\partial t} = \left[k_{12}\frac{k_0}{k_1} - \tilde{k}_1\right]\tilde{p} - \frac{k_{12}^2\,k_0}{k_1^2}\,\tilde{p}^2\,. \tag{8}$$

For convenience, instead of working with the absolute amount of misfolded protein $\tilde{p}$, we scale equation (8) by the maximum amount of misfolded protein $\tilde{p}^{\max} = k_1/k_{12}\,[\,1 - [k_1\tilde{k}_1]/[k_0 k_{12}]\,]$, and re-parameterize equation (8) in terms of the misfolded protein concentration $c = \tilde{p}\ /\tilde{p}^{\max}$, which varies between zero and one, $0 \le c \le 1$,

$$\frac{\partial c}{\partial t} = f^c \quad \text{with} \quad f^c = \left[k_{12}\frac{k_0}{k_1} - \tilde{k}_1\right] c\,[\,1 - c\,]\,. \tag{9}$$

This definition implies that the spatial reaction or source term f^c is directly correlated to the kinetics of misfolding in Eq. (6): The misfolded protein concentration c increases linearly with the conversion rate from the healthy to the misfolded conformation k_{12} and with the equilibrium concentration of healthy protein $p_0 = k_0/k_1$, and decreases linearly with the clearance of misfolded protein $\tilde{k}_1$.

Remark 1 (*Fisher–Kolmogorov equation*)**.** The reaction–diffusion equation for the growth and spreading of misfolded proteins (2) with a nonlinear reaction term ((9).2) of $\alpha\,c\,[1-c]$-type is broadly known as the Fisher–Kolmogorov equation [24,25]. It was originally proposed to model the spreading of a favored gene in population dynamics, and is now widely used to describe traveling wave solutions in ecology, physiology, combustion, crystallization, plasma physics, and phase transition. Here the parameter $\alpha = k_{12}k_0/k_1 - \tilde{k}_1$ follows naturally from the kinetics of misfolding (6). A characteristic feature of the Fisher–Kolmogorov equation is that the amount of misfolded protein, once seeded anywhere in the domain, $c > 0$, will always increase, $c \to 1$, and never return back to the benign state, $c = 0$.

For the flux $\boldsymbol{q}$, we assume that spreading is driven by the spatial concentration gradient $\nabla_x c$ and occurs by two distinct mechanisms, extracellular diffusion d^{ext}, which we associate with the isotropic diffusion through the extracellular space, and axonal transport d^{axn}, which we associate with the local axonal direction $\boldsymbol{n}$,

$$J\,\boldsymbol{q} = \boldsymbol{d}\cdot\nabla_x c \quad \text{with} \quad \boldsymbol{d} = d^{\text{ext}}\,\boldsymbol{i} + d^{\text{axn}}\,\boldsymbol{n}\otimes\boldsymbol{n}/\lambda_{\text{n}}^2\,. \tag{10}$$

Here $\boldsymbol{i}$ is the spatial identity tensor, $\boldsymbol{n}/\lambda_{\text{n}} = \boldsymbol{F}\cdot\boldsymbol{n}_0/\lambda_{\text{n}}$ is the current axonal unit vector, $\boldsymbol{n}_0$ is the initial axonal unit vector that we can determine from diffusion tensor magnetic resonance elastography, and $\lambda_{\text{n}} = \|\,\boldsymbol{F}\cdot\boldsymbol{n}_0\,\|$ is its stretch upon deformation. We can rephrase the source $J\,f^c = F^c$ and flux $J\,\boldsymbol{q} = \boldsymbol{Q}\cdot\boldsymbol{F}^{\text{t}}$, and introduce the material source F^c and flux $\boldsymbol{Q}$ in terms of the material concentration gradient $\nabla_X c$ and the material diffusion tensor $\boldsymbol{D} = \boldsymbol{F}^{-1}\cdot\boldsymbol{d}\cdot\boldsymbol{F}^{-\text{t}}$,

$$F^c = J\left[k_{12}\frac{k_0}{k_1} - \tilde{k}_1\right] c\,[\,1-c\,] \quad \text{and} \quad \boldsymbol{Q} = \boldsymbol{D}\cdot\nabla_X c \quad \text{with} \quad \boldsymbol{D} = d^{\text{ext}}\,\boldsymbol{C}^{-1} + d^{\text{axn}}\,\boldsymbol{n}_0\otimes\boldsymbol{n}_0/\lambda_{\text{n}}^2\,, \tag{11}$$

where $\boldsymbol{C} = \boldsymbol{F}^{\text{t}}\cdot\boldsymbol{F}$ is the right Cauchy Green deformation tensor and $\boldsymbol{C}^{-1} = \boldsymbol{F}^{-1}\cdot\boldsymbol{F}^{-\text{t}}$ is its inverse. The constitutive equation for the flux $\boldsymbol{Q}$ illustrates that the protein spreading problem is constitutively coupled to the tissue atrophy problem through the deformation-dependent flux $\boldsymbol{Q}$ in Eq. (11) via $\boldsymbol{C}^{-1}$ and $\lambda_{\text{n}} = \|\,\boldsymbol{F}\cdot\boldsymbol{n}_0\,\|$.

Remark 2 (*Constitutive decoupling*)**.** When defining the source f^c in (9) and the flux $\boldsymbol{q}$ in (10) in the current configuration, we introduce an implicit coupling between the protein spreading problem and the tissue atrophy problem. Alternatively, we could define the source F^c,

$$F^c = \left[k_{12}\frac{k_0}{k_1} - \tilde{k}_1\right] c\,[\,1-c\,]\,, \tag{12}$$

and the flux $\boldsymbol{Q}$ in the initial configuration as functions of the material diffusion tensor $\boldsymbol{D}$, the material unit tensor $\boldsymbol{I}$, the initial axonal unit vector $\boldsymbol{n}_0$, and the material gradient of the concentration $\nabla_X c$,

$$\boldsymbol{Q} = \boldsymbol{D} \cdot \nabla_X c \quad \text{with} \quad \boldsymbol{D} = D^{\text{ext}}\, \boldsymbol{I} + D^{\text{axn}}\, \boldsymbol{n}_0 \otimes \boldsymbol{n}_0 \,. \tag{13}$$

We can then rephrase the source $F^c = J\, f^c$ and flux $\boldsymbol{Q} = J\, \boldsymbol{q} \cdot \boldsymbol{F}^{-\text{t}}$, and introduce the spatial source f^c and flux $J\boldsymbol{q}$ in terms of the spatial concentration gradient $\nabla_x c$ and the spatial diffusion tensor $\boldsymbol{d} = \boldsymbol{F} \cdot \boldsymbol{D} \cdot \boldsymbol{F}^{\text{t}}$,

$$f^c = \frac{1}{J} \left[k_{12}\, \frac{k_0}{k_1} - \tilde{k}_1 \right] c\,[\,1 - c\,] \quad \text{and} \quad \boldsymbol{q} = \frac{1}{J}\, \boldsymbol{d} \cdot \nabla_x c \quad \text{with} \quad \boldsymbol{d} = D^{\text{ext}}\, \boldsymbol{b} + D^{\text{axn}}\, \boldsymbol{n} \otimes \boldsymbol{n} \,, \tag{14}$$

where $\boldsymbol{b} = \boldsymbol{F} \cdot \boldsymbol{F}^{\text{t}}$ is the left Cauchy Green deformation tensor. Obviously, the materially defined source (12) and flux (13) are different from the pull back of the spatially defined source and flux (11), and the spatially defined source (9) and flux (10) are different from the push forward of the materially defined source and flux (14). The most notable difference is that the materially defined source (12) and flux (13) are deformation independent and no longer coupled to the tissue atrophy problem. The extent by which the spatially and materially defined fluxes differ depends on the degree of atrophy ϑ and on the time delay between protein misfolding and the onset of atrophy. In other words, a sufficient time delay between protein misfolding and tissue atrophy would justify using the material constitutive equations (12) and (13) and solving the protein spreading and tissue atrophy problems in a decoupled way.

Constitutive equations of tissue atrophy. For the tissue atrophy problem, we have to define constitutive equations for the atrophy tensor $\boldsymbol{F}^{\text{a}}$ and the Piola stress $\boldsymbol{P}$ or Cauchy stress $\boldsymbol{\sigma}$. We assume that gray matter atrophy is purely isotropic,

$$\boldsymbol{F}^{\text{a}} = \sqrt[3]{\vartheta}\, \boldsymbol{I} \quad \text{and} \quad \boldsymbol{F}^{\text{e}} = \boldsymbol{F} \,/ \sqrt[3]{\vartheta} \,, \tag{15}$$

and that white matter atrophy is anisotropic and reflects thinning of cortical fiber tracts orthogonal to the fiber direction $\boldsymbol{n}_0$,

$$\boldsymbol{F}^{\text{a}} = \sqrt{\vartheta}\, \boldsymbol{I} + [\,1 - \sqrt{\vartheta}\,]\, \boldsymbol{n}_0 \otimes \boldsymbol{n}_0 \quad \text{and} \quad \boldsymbol{F}^{\text{e}} = \boldsymbol{F} / \sqrt{\vartheta} + [1 - 1/\sqrt{\vartheta}]\, \boldsymbol{n} \otimes \boldsymbol{n}_0 \,. \tag{16}$$

By design, in both cases, ϑ is a measure of the volume loss or tissue shrinkage J^{a},

$$\vartheta = J^{\text{a}} \quad \text{and} \quad J^{\text{e}} = J \,/\, \vartheta \,. \tag{17}$$

We propose a novel constitutive model for brain atrophy in which the tissue atrophies naturally at a rate G_0. We assume that an increase in misfolded protein c accelerates the progression of natural atrophy by a factor $\gamma(c)$. For simplicity, we assume that $\gamma(c)$ is the product of atrophy acceleration G_c/G_0 and the Heaviside step function $\mathcal{H}(c - c^{\text{crit}})$, which activates atrophy acceleration once the misfolded protein concentration c exceeds a critical threshold c^{crit},

$$\dot{\vartheta} = [\,1 + \gamma(c)\,]\, G_0 = \begin{cases} G_0 & \text{if} \quad c < c^{\text{crit}} \\ G_0 + G_c & \text{if} \quad c \geq c^{\text{crit}} \end{cases} \quad \text{where} \quad \gamma(c) = \frac{G_c}{G_0}\, \mathcal{H}(c - c^{\text{crit}}) \,. \tag{18}$$

This implies that we can interpret G_0 and G_c as the natural and the misfolding induced atrophy rates. To characterize the mechanical behavior of the tissue, we introduce the neo-Hookean free energy ψ_0 as the atrophy-weighted elastic stored energy ψ, which depends exclusively on the elastic part of the deformation,

$$\psi_0 = J^{\text{a}}\, \psi \quad \text{with} \quad \psi = \tfrac{1}{2}\, \mu\, [\, \boldsymbol{F}^{\text{e}} : \boldsymbol{F}^{\text{e}} - 3 - 2\, \ln(J^{\text{e}})\,] + \tfrac{1}{2}\, \lambda\, \ln^2(J^{\text{e}}) \,. \tag{19}$$

Here μ and λ are the standard Lamé parameters that relate to the Young's modulus E and Poisson's ratio ν in the linear limit as $\lambda = E\nu/[[1+\nu][1-2\nu]]$ and $\mu = E/[2[1+\nu]]$. Here we assume $\mu = 2.07\,\text{kPa}$ and $\lambda = 101.43\,\text{kPa}$ for gray and $\mu = 1.15\,\text{kPa}$ and $\lambda = 56.35\,\text{kPa}$ for white matter [26]. Following standard arguments of thermodynamics, we obtain the Cauchy stress $\boldsymbol{\sigma}$,

$$\boldsymbol{\sigma} = \frac{1}{J}\, \frac{\text{d}\psi_0}{\text{d}\boldsymbol{F}} \cdot \boldsymbol{F}^{\text{t}} = \frac{1}{J^{\text{e}}}\, \frac{\text{d}\psi}{\text{d}\boldsymbol{F}^{\text{e}}} \cdot (\boldsymbol{F}^{\text{e}})^{\text{t}} = \frac{1}{J^{\text{e}}} [\, \mu\, \boldsymbol{F}^{\text{e}} \cdot (\boldsymbol{F}^{\text{e}})^{\text{t}} + [\, \lambda\, \ln(J^{\text{e}}) - \mu\,]\, \boldsymbol{i}\,] \,, \tag{20}$$

from the neo-Hookean free energy ψ_0 in Eq. (19). We emphasize that the Cauchy stress is parameterized exclusively in terms of the elastic tensor $\boldsymbol{F}^{\text{e}}$ and its Jacobian J^{e}.

3. Computational modeling of protein spreading and tissue atrophy

Continuous residuals. We solve the protein spreading and tissue atrophy problems using the finite element method and rephrase equations (3) and (5) in their residual forms,

$$\begin{aligned} \mathsf{R}^c &= \dot{c} - \operatorname{div}\boldsymbol{q} - f^c \doteq 0 \quad \text{in } \mathcal{B}_t \\ \mathbf{R}^\varphi &= \operatorname{div}\boldsymbol{\sigma} + \boldsymbol{f}^\varphi \doteq \mathbf{0} \quad \text{in } \mathcal{B}_t\,. \end{aligned} \tag{21}$$

To obtain the weak forms of the residuals (21), we multiply them with the test functions δc and $\delta\boldsymbol{\varphi}$, integrate them over the domain $\mathcal{B}_t$, perform integration by parts, and use the Neumann boundary conditions.

Spatial and temporal discretizations. In the spirit of the finite element method, we discretize the misfolded protein concentration c and the deformation $\boldsymbol{\varphi}$ as global degrees of freedom at the node point level and introduce the degree of atrophy ϑ as an internal variable on the integration point level. For the spatial discretization, we discretize the domain $\mathcal{B}_t$ into n_{el} finite elements, such that $\mathcal{B}_t = \bigcup_{e=1}^{n_{\text{el}}} \mathcal{B}_t^e$. We use $\mathcal{C}^0$-continuous shape functions to interpolate the test and trial functions of the concentration δc and c and of the deformation $\delta\boldsymbol{\varphi}$ and $\boldsymbol{\varphi}$,

$$\delta c = \sum_{i=1}^{n_{\text{en}}} N_i^c\,\delta c_i \qquad c = \sum_{k=1}^{n_{\text{en}}} N_k^c\,c_k \qquad \delta\boldsymbol{\varphi} = \sum_{j=1}^{n_{\text{en}}} N_j^\varphi\,\delta\boldsymbol{\varphi}_j \qquad \boldsymbol{\varphi} = \sum_{l=1}^{n_{\text{en}}} N_l^\varphi\,\boldsymbol{\varphi}_l \tag{22}$$

where i, j, k, l sum over the n_{en} element nodes. Although we could technically use different orders of interpolation, here we use the same shape functions N for the concentration c and the deformation $\boldsymbol{\varphi}$. For the temporal discretization, we partition the time interval of interest $\mathcal{T}$ into n_{step} discrete subintervals $[\,t_n, t_{n+1}\,]$, such that $\mathcal{T} = \bigcup_{n=0}^{n_{\text{step}}-1} [\,t_n, t_{n+1}\,]$. We assume that we know the concentration c_n, the deformation $\boldsymbol{\varphi}_n$, the atrophy ϑ_n and all derivable quantities at the beginning of the current interval. In the spirit of implicit time integration schemes, we adopt a finite difference scheme to approximate the evolution of the misfolded protein concentration c in the discrete residual ((21).1) and the evolution of atrophy ϑ in Eq. (18) as follows,

$$\dot{c} = [\,c - c_n\,]/\Delta t \quad \text{and} \quad \dot{\vartheta} = [\,\vartheta - \vartheta_n\,]/\Delta t\,, \tag{23}$$

where $(\circ)$ and $(\circ)_n$ denote the unknown quantities at $t = t_{n+1}$ and t_n, and $\Delta t = t - t_n > 0$ is the current time increment. At the integration point level, for the current concentration c, we evaluate the time-discrete evolution of the atrophy, $\vartheta = \vartheta_n + [\,1 + \gamma(c)\,]\,G_0\,\Delta t$ from Eq. (18) with ((23).3), calculate the atrophy tensor $\boldsymbol{F}^{\text{a}}$ and the elastic tensor $\boldsymbol{F}^{\text{e}}$ from Eqs. (15) or (16), and determine the Cauchy stress $\boldsymbol{\sigma}$ from Eq. (20).

Algorithmic residuals. By multiplying the continuous residuals (21) with the test functions δc and $\delta\boldsymbol{\varphi}$, integrating them over the domain $\mathcal{B}_t$, performing integration by parts, and using the spatial (22) and temporal (23) discretizations, we obtain the discrete algorithmic residuals of the protein spreading and tissue atrophy problems,

$$\begin{aligned} \mathsf{R}_I^c &= \mathop{\mathbf{A}}_{e=1}^{n_{\text{el}}} \int_{\mathcal{B}_t^e} N_i^c \left[\frac{c - c_n}{\Delta t}\right] + \nabla_{\boldsymbol{x}} N_i^c \cdot \boldsymbol{q} - N_i^c\, f^c \;\mathrm{d}v \doteq 0 \\ \mathbf{R}_J^\varphi &= \mathop{\mathbf{A}}_{e=1}^{n_{\text{el}}} \int_{\mathcal{B}_t^e} \nabla_{\boldsymbol{x}} N_j^\varphi \cdot \boldsymbol{\sigma} - N_j^\varphi\, \boldsymbol{f}^\varphi \;\mathrm{d}v \doteq \mathbf{0}\,, \end{aligned} \tag{24}$$

where the operator $\mathbf{A}_{e=1}^{n_{\text{el}}}$ symbolizes the assembly of the element residuals at the n_{en} element nodes i and j to the overall residuals at the n_{gn} global nodes I and J.

Linearization. We solve the discrete algorithmic residuals (24) using the incremental iterative Newton–Raphson method and linearize the residuals,

$$\begin{aligned} \mathsf{R}_I^c &+ \sum_{K=1}^{n_{\text{gn}}} \mathsf{K}_{IK}^{cc}\,\mathrm{d}c_K + \sum_{L=1}^{n_{\text{gn}}} \mathbf{K}_{IL}^{c\varphi} \cdot \mathrm{d}\boldsymbol{\varphi}_L \doteq 0 \\ \mathbf{R}_J^\varphi &+ \sum_{K=1}^{n_{\text{gn}}} \mathbf{K}_{JK}^{\varphi c}\,\mathrm{d}c_K + \sum_{L=1}^{n_{\text{gn}}} \mathbf{K}_{JL}^{\varphi\varphi} \cdot \mathrm{d}\boldsymbol{\varphi}_L \doteq \mathbf{0} \end{aligned} \tag{25}$$

to obtain the iterative update equations for the incremental unknowns $\mathrm{d}c_K$ and $\mathrm{d}\boldsymbol{\varphi}_L$ in terms of the following tangent moduli,

$$\begin{aligned}
\mathsf{K}^{cc}_{IK} &= \frac{\mathrm{d}\mathsf{R}^c_I}{\mathrm{d}c_K} = \mathop{\mathsf{A}}_{e=1}^{n_{\text{el}}} \int_{\mathcal{B}^e_t} N^c_i \left[\frac{1}{\Delta t}\right] N^c_k + \nabla_{\boldsymbol{x}} N^c_i \cdot \left[\frac{\mathrm{d}\boldsymbol{q}}{\mathrm{d}\nabla_{\boldsymbol{x}} c}\right] \cdot \nabla_{\boldsymbol{x}} N^c_k + N^c_i \left[\frac{\mathrm{d}f^c}{\mathrm{d}c}\right] N^c_k \, \mathrm{d}v \\
\mathbf{K}^{c\varphi}_{IL} &= \frac{\mathrm{d}\mathsf{R}^c_I}{\mathrm{d}\boldsymbol{\varphi}_L} = \mathop{\mathsf{A}}_{e=1}^{n_{\text{el}}} \int_{\mathcal{B}^e_t} \nabla_{\boldsymbol{x}} N^c_i \cdot \boldsymbol{q} \, \nabla_{\boldsymbol{x}} N^\varphi_l + \nabla_{\boldsymbol{x}} N^c_i \cdot \left[\frac{\mathrm{d}\boldsymbol{q}}{\mathrm{d}\boldsymbol{F}}\right] \cdot \boldsymbol{F}^{\mathrm{t}} \cdot \nabla_{\boldsymbol{x}} N^\varphi_l \, \mathrm{d}v \\
\mathbf{K}^{\varphi c}_{JK} &= \frac{\mathrm{d}\mathbf{R}^\varphi_J}{\mathrm{d}c_K} = \mathop{\mathsf{A}}_{e=1}^{n_{\text{el}}} \int_{\mathcal{B}^e_t} \nabla_{\boldsymbol{x}} N^\varphi_j \cdot \left[\frac{\mathrm{d}\boldsymbol{\sigma}}{\mathrm{d}c}\right] N^c_k \, \mathrm{d}v \\
\mathbf{K}^{\varphi\varphi}_{JL} &= \frac{\mathrm{d}\mathbf{R}^\varphi_J}{\mathrm{d}\boldsymbol{\varphi}_L} = \mathop{\mathsf{A}}_{e=1}^{n_{\text{el}}} \int_{\mathcal{B}^e_t} \nabla_{\boldsymbol{x}} N^\varphi_j \cdot \boldsymbol{\sigma} \cdot \nabla_{\boldsymbol{x}} N^\varphi_l \, \boldsymbol{i} + \nabla_{\boldsymbol{x}} N^\varphi_j \cdot \mathbf{c} \cdot \nabla_{\boldsymbol{x}} N^\varphi_l \, \mathrm{d}v \,.
\end{aligned} \tag{26}$$

The concentration moduli K^{cc}_{IK} consist of three terms associated with the temporal evolution, the spreading, and the growth of misfolded protein. The mixed moduli $\mathbf{K}^{c\varphi}_{IL}$ reflect the influence of the deformation $\boldsymbol{\varphi}$ on the spreading of misfolded protein c, where the first and second terms associated with the geometric and constitutive contributions. The mixed moduli $\mathbf{K}^{\varphi c}_{JK}$ reflect the influence of the misfolded protein concentration c on tissue atrophy $\boldsymbol{F}^{\mathrm{a}}$, which indirectly influences the elastic tensor $\boldsymbol{F}^{\mathrm{e}}$, and with it the mechanical stress $\boldsymbol{\sigma}$. The mechanical moduli $\mathbf{K}^{\varphi\varphi}_{JL}$, similar to the mixed moduli $\mathbf{K}^{c\varphi}_{IL}$, consist of a geometric and a constitutive contribution, where the latter includes the fourth order tensor of constitutive moduli $\mathbf{c}$ that reflect the dependence of the mechanical stress $\boldsymbol{\sigma}$ on the deformation $\boldsymbol{\varphi}$.

From the sensitivities of flux $\boldsymbol{q}$ and source f^c with respect to the misfolded protein concentration c and its gradient $\nabla_{\boldsymbol{x}} c$ we obtain the derivatives for the tangent moduli K^{cc}_{IK},

$$\frac{\mathrm{d}\boldsymbol{q}}{\mathrm{d}\nabla_{\boldsymbol{x}} c} = \frac{1}{J}\,[\, d^{\text{ext}}\boldsymbol{i} + d^{\text{axn}}\boldsymbol{n}\otimes\boldsymbol{n}/\lambda_{\text{n}}^2\,] \qquad \text{and} \qquad \frac{\mathrm{d}f^c}{\mathrm{d}c} = \left[k_{12}\,\frac{k_0}{k_1} - \tilde{k}_1\right][\,1-2c\,]\,. \tag{27}$$

From the sensitivity of the flux $\boldsymbol{q}$ with respect to the deformation gradient $\boldsymbol{F}$ we obtain the derivative for the tangent moduli $\mathbf{K}^{c\varphi}_{IL}$,

$$\frac{\mathrm{d}\boldsymbol{q}}{\mathrm{d}\boldsymbol{F}} \cdot \boldsymbol{F}^{\mathrm{t}} = \frac{1}{J}\, d^{\text{axn}}\,[\,\boldsymbol{i}\otimes\boldsymbol{n} + \boldsymbol{n}\otimes\boldsymbol{i} - 2\,\boldsymbol{n}\otimes\boldsymbol{n}\otimes\boldsymbol{n}/\lambda_{\text{n}}\,]\cdot\nabla_{\boldsymbol{x}} c\otimes\boldsymbol{n}/\lambda_{\text{n}}^2 - \boldsymbol{q}\otimes\boldsymbol{i}\,. \tag{28}$$

From the sensitivity of the Cauchy stress $\boldsymbol{\sigma}$ with respect to the misfolded protein concentration c, along with the abbreviation $\boldsymbol{A} = [\mathrm{d}\boldsymbol{F}^{\mathrm{a}}/\mathrm{d}\vartheta][\mathrm{d}\vartheta/\mathrm{d}c]$ with either $\mathrm{d}\boldsymbol{F}^{\mathrm{a}}/\mathrm{d}\vartheta = 1/[3\,\sqrt[3]{\vartheta^2}]\,\boldsymbol{I}$ from (15) or $\mathrm{d}\boldsymbol{F}^{\mathrm{a}}/\mathrm{d}\vartheta = 1/[2\,\sqrt{\vartheta}]\,[\,\boldsymbol{I} - \boldsymbol{n}_0\otimes\boldsymbol{n}_0]$ from (16) and $[\mathrm{d}\vartheta/\mathrm{d}c] = [\mathrm{d}\gamma/\mathrm{d}c]\,G_0\,\Delta t$ from (18), we obtain the derivative for the tangent moduli $\mathbf{K}^{\varphi c}_{JK}$,

$$\frac{\mathrm{d}\boldsymbol{\sigma}}{\mathrm{d}c} = \frac{\mathrm{d}\boldsymbol{\sigma}}{\mathrm{d}\boldsymbol{F}^{\mathrm{a}}} : \frac{\mathrm{d}\boldsymbol{F}^{\mathrm{a}}}{\mathrm{d}c} = -[\boldsymbol{F}^{\mathrm{e}}\cdot\boldsymbol{A}\cdot\boldsymbol{F}^{-1}]\cdot\boldsymbol{\sigma} + [\boldsymbol{A} : (\boldsymbol{F}^{\mathrm{a}})^{-\mathrm{t}}]\,\boldsymbol{\sigma} - \mathbf{c} : [\boldsymbol{F}^{\mathrm{e}}\cdot\boldsymbol{A}\cdot(\boldsymbol{F}^{\mathrm{a}})^{-1}]\,. \tag{29}$$

From the sensitivity of the Cauchy stress $\boldsymbol{\sigma}$ with respect to the deformation gradient $\boldsymbol{F}$ along with the associated symmetry requirements we obtain the standard fourth-order tensor $\mathbf{c}$ of the spatial moduli of the neo-Hookean model for the tangent moduli $\mathbf{K}^{\varphi\varphi}_{JL}$,

$$\mathbf{c} = \frac{1}{J^{\mathrm{e}}}\,[\boldsymbol{i}\,\overline{\otimes}\,\boldsymbol{F}^{\mathrm{e}}] : \frac{\partial^2\psi}{\partial\boldsymbol{F}^{\mathrm{e}}\otimes\partial\boldsymbol{F}^{\mathrm{e}}} : [\boldsymbol{i}\,\overline{\otimes}\,(\boldsymbol{F}^{\mathrm{e}})^{\mathrm{t}}] = \frac{1}{J^{\mathrm{e}}}[\,\mu - \lambda\ln(J^{\mathrm{e}})\,][\,\boldsymbol{i}\,\overline{\otimes}\,\boldsymbol{i} + \boldsymbol{i}\,\underline{\otimes}\,\boldsymbol{i}\,] + \lambda\,\boldsymbol{i}\otimes\boldsymbol{i}\,, \tag{30}$$

where the component representations of the non-standard fourth-order products expand as $\{\bullet\,\overline{\otimes}\,\circ\}_{ijkl} = \{\bullet\}_{ik}\otimes\{\circ\}_{jl}$ and $\{\bullet\,\underline{\otimes}\,\circ\}_{ijkl} = \{\bullet\}_{il}\otimes\{\circ\}_{jk}$. For each time increment Δt, we solve equations (25) for the iterative updates of the global unknowns, $\mathrm{d}c$ and $\mathrm{d}\boldsymbol{\varphi}$, and update the incremental unknowns, $\Delta c \leftarrow \Delta c + \mathrm{d}c$ and $\Delta\boldsymbol{\varphi} \leftarrow \Delta\boldsymbol{\varphi} + \mathrm{d}\boldsymbol{\varphi}$, until we achieve global convergence.

Remark 3 (*Constitutive decoupling*)**.** Defining the constitutive equation for the spatial flux $\boldsymbol{q}$ rather than the material flux $\boldsymbol{Q}$ introduces the $\boldsymbol{q}$ and $[\mathrm{d}\boldsymbol{q}/\mathrm{d}\boldsymbol{F}]\cdot\boldsymbol{F}^{\mathrm{t}}$ terms in the tangent moduli ((26).2). If we define the constitutive equations for the material flux $\boldsymbol{Q}$ as functions of the material diffusion tensor $\boldsymbol{D}$, the initial axonal unit vector $\boldsymbol{n}_0$, and the material concentration gradient $\nabla_X c$ as proposed in (13), the above coupling terms will vanish, and the protein spreading problem ((24).1) decouples from the tissue atrophy problem ((24).2). We can then solve the protein spreading problem first, record the concentration c to update the degree of atrophy ϑ using Eq. (18), and then solve the tissue atrophy problem.

Remark 4 (*Implementation in Abaqus/Standard*)**.** To solve the discrete algorithmic residuals (24), we can use the analogies of our protein spreading problem (2) or (3) and the classical nonlinear heat transfer problem [27] and interpret the protein concentration c as temperature scaled to $0 \leq c \leq 1$, the concentration flux $\boldsymbol{q}$ as heat flux, and the diffusion tensor $\boldsymbol{d}$ as conductivity tensor, and the nonlinear source f^c as heat source. In Abaqus/Standard, we can add this nonlinear source to the standard heat transfer problem using the subroutine HETVAL, where we define $f^c = \alpha\, c\,[1-c]$ and $\mathrm{d}f^c/\mathrm{d}c = \alpha\,[1-2\,c]$ with $\alpha = k_{12}k_0/k_1 - \tilde{k}_1$. We can then solve the protein spreading and tissue atrophy problems as a coupled problem using a thermo-mechanical formulation with a user-defined subroutine UMAT where we discretize the degree of atrophy ϑ as an internal variable at the integration point level. At each integration point, we update the degree of atrophy according to $\vartheta = \vartheta_n + [\,1 + \gamma(c)\,]\,G_0\,\Delta t$, here specifically $\vartheta = \vartheta_n + [\,G_0 + G_c\,\mathcal{H}(c - c^{\text{crit}})\,]\,\Delta t$ from Eq. (18), calculate the atrophy tensor $\boldsymbol{F}^{\text{a}}$ and the elastic tensor $\boldsymbol{F}^{\text{e}}$ from Eq. (15) or (16), calculate the Cauchy stress $\boldsymbol{\sigma}$ from Eq. (20), and calculate the sensitivities from Eqs. (27) to (30). However, rather than working directly with the constitutive moduli $\mathbf{c}$ from Eq. (30), the user-defined subroutine in Abaqus/Standard utilizes the Jauman rate of the Cauchy stress [27], which requires the following modification of the tangent moduli, $\mathbf{c}^{\text{abaqus}} = \mathbf{c} + \frac{1}{2}\,[\,\boldsymbol{\sigma} \,\overline{\otimes}\, \boldsymbol{I} + \boldsymbol{I} \,\overline{\otimes}\, \boldsymbol{\sigma} + \boldsymbol{\sigma} \,\underline{\otimes}\, \boldsymbol{I} + \boldsymbol{I} \,\underline{\otimes}\, \boldsymbol{\sigma}\,]$.

Brain models. We created six two-dimensional finite element models from T2 weighted magnetic resonance images of a healthy adult female brain using MATLAB and the mesh generator gmsh [28]. We selected one sagittal and one coronal slice and generated three linear triangular meshes with varying average mesh size h for each slice. Fig. 3 illustrates the resulting geometries and number of elements. The coronal models consist of 2646 nodes and 4710 elements with an average mesh size of $h = 2.5\,\text{mm}$, 6282 nodes and 11,596 elements with $h = 1.5\,\text{mm}$, and 13,245 nodes and 25,037 elements with $h = 1.0\,\text{mm}$. The sagittal models consist of 3163 nodes and 4690 elements with an average mesh size of $h = 2.5\,\text{mm}$, 7760 nodes and 11,838 elements with $h = 1.5\,\text{mm}$, and 16,260 nodes and 25,812 elements with $h = 1.0\,\text{mm}$.

Tractography models. To obtain the element-wise fiber orientations for the anisotropic diffusion coefficient and anisotropic tissue atrophy, we infer a small number of idealized fibers from tractography illustrations in the literature [29–31] and project them onto our two-dimensional meshes. Fig. 4, top, illustrates these idealized fiber directions. In a next step, we detect the elements crossed by fibers in MATLAB and assign them the corresponding orientation vectors. Subsequently, we use a fast marching algorithm to propagate the orientations through the entire mesh. We perform several iterations until every element is provided with its own orientation. We create a list with element numbers and matching orientation unit vectors as an input to our finite element simulations. Fig. 4, bottom, shows our tractography models of the axonal fiber network, generated from the element-wise fiber orientations using Paraview's Stream Tracer feature [32]. The resulting images are in excellent agreement with the tractography data we used as input for our algorithm [29–31].

Initial and boundary conditions. For the initial conditions, we initiate the spreading of misfolded tau protein by elevating the initial concentration to $c_0^* = 0.8$ in a small seeding region $\mathcal{B}^*$. We set the initial concentration equal to zero $c_0 = 0.0$ in all other regions $\mathcal{B} \setminus \mathcal{B}^*$. We infer the seeding region $\mathcal{B}^*$ from the post-mortem analysis of brains with Alzheimer's disease [4]. In the coronal model we seed misfolded protein in the transentorhinal cortex. This region is located in the temporal lobes and is not explicitly part of our sagittal section. In the sagittal model, we seed misfolded protein in the nodes which are connected most closely to the temporal lobe [29]. For the boundary conditions, we assume that no misfolded protein can leave the system and apply homogeneous Neumann boundary conditions for the protein spreading problem. We assume that the brain shrinks downward towards the stem and apply homogeneous Dirichlet boundary conditions for the tissue atrophy problem in a small region close to the brain stem. To allow for a comparison with longitudinal magnetic resonance imaging studies, we simulate a period of 15 years with a time increment of $\Delta t = 0.05$ years. At each time point, we calculate the degree of tissue atrophy and assume that the original brain volume corresponds to 85% of the total intracranial volume [19]. We compare these data to the reported volume changes from longitudinal magnetic resonance imaging studies from Fig. 1.

Mesh convergence study. To determine the adequate mesh size we conduct a mesh convergence study. We perform the simulations with a fixed set of model parameters for our three average mesh sizes of $h = 2.5\,\text{mm}$, $h = 1.5\,\text{mm}$, and $h = 1.0\,\text{mm}$. For both the coronal and sagittal models, we adjust the number of seeding nodes with $c^* = 0.8$ to ensure equally sized seeding regions for all six cases and compare the resulting degree of tissue atrophy. For all

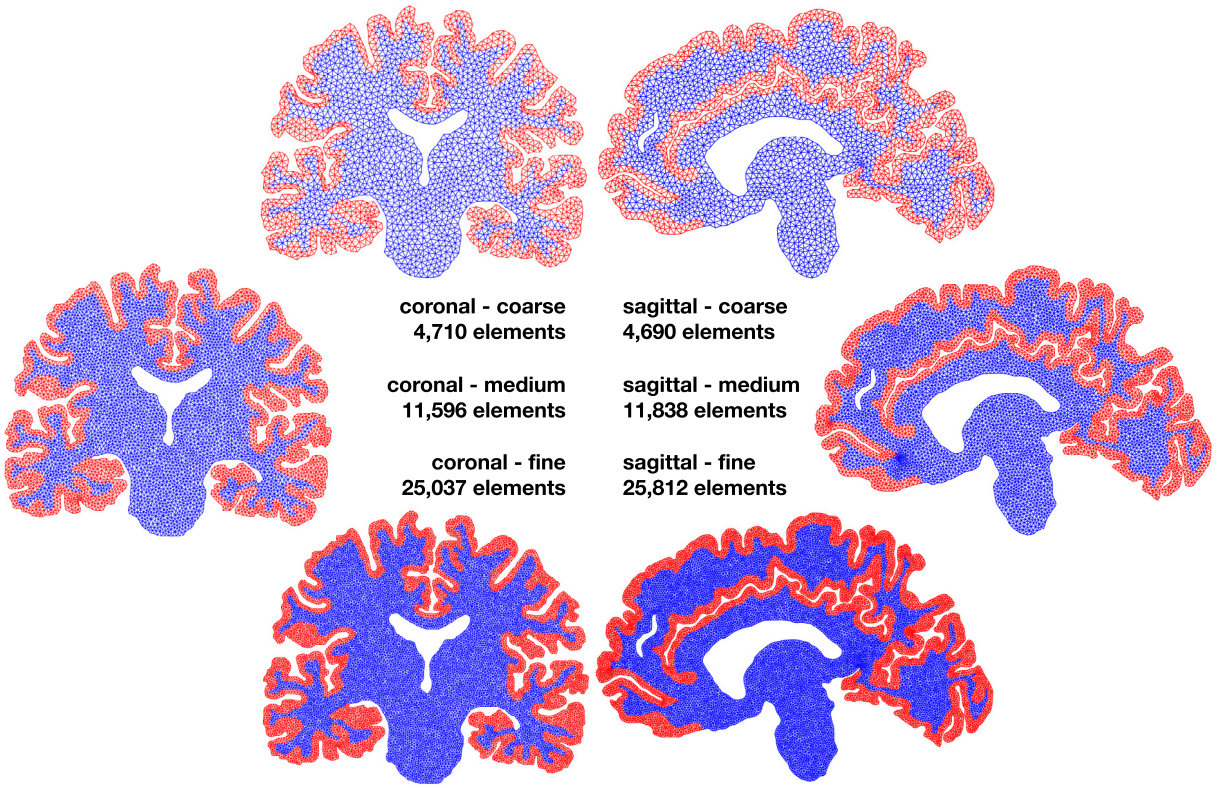

Fig. 3. Coronal and sagittal models with varying mesh sizes. The coarse models have an average element size of $h = 2.5$ mm and consist of 4710 and 4690 elements; the medium models have an average element size of $h = 1.5$ mm and consist of 11,596 and 11,838 elements; and the fine models have an average element size of $h = 1.0$ mm and consist of 25,037 and 25,812 elements.

subsequent simulations, we select the coarsest mesh size for which the results converge both for the coronal and sagittal models.

Sensitivity analysis. Our model of protein spreading and tissue atrophy introduces six model parameters: the critical concentration c^{crit} which initiates atrophy, the extracellular diffusion d^{ext}, the axonal transport d^{axn}, the production of misfolded protein $\alpha = k_{12}\,k_0/k_1 - \tilde{k}_1$, and the misfolded-protein-induced atrophy in gray and white matter G_c^{gray} and G_c^{white}. For simplicity, we assume that axonal transport is ten times faster than extracellular diffusion, $d^{\text{axn}} : d^{\text{ext}} = 10 : 1$. We fix the natural atrophy rate at $G_0 = -0.01$ /year, and the ratio between the gray and white matter atrophy rates at $\dot{\vartheta}^{\text{gray}} : \dot{\vartheta}^{\text{white}} = 3 : 2$ [15]. We systematically vary all other parameters, and compare the resulting tissue atrophy curves to the curve in Fig. 1 to visualize how the individual model parameters affect the overall neurodegenerative response. From these sensitivity analyses, we selected a set of parameters for which we extract contour plots of the misfolded protein concentration c, the tissue atrophy $J^{\text{a}} = \vartheta$, and von Mises stresses σ at selected points in time.

4. Results

4.1. Mesh convergence study

Fig. 5 shows the results of our mesh convergence study. For the coronal model, the simulations with the coarse mesh with an average mesh size of $h = 2.5$ mm, the medium mesh with $h = 1.5$ mm, and the fine mesh with $h = 1.0$ cm show minor variations in predicted relative brain volume towards late stages of atrophy. For the sagittal model, in contrast, all three mesh sizes predict similar results. Consequently, we choose the medium coronal model and the medium sagittal model for all subsequent simulations.

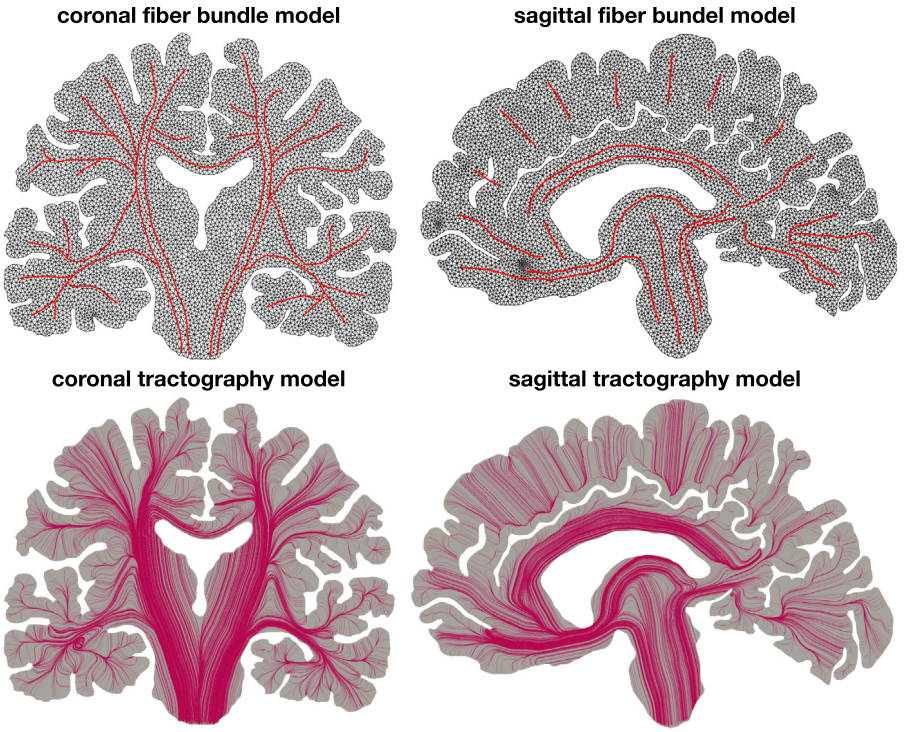

Fig. 4. Coronal and sagittal fiber bundle models and tractography models. Fiber bundle models highlight the idealized fiber orientations as red lines plotted on the medium mesh. Tractography models illustrate the streamlines of the axonal fiber network.

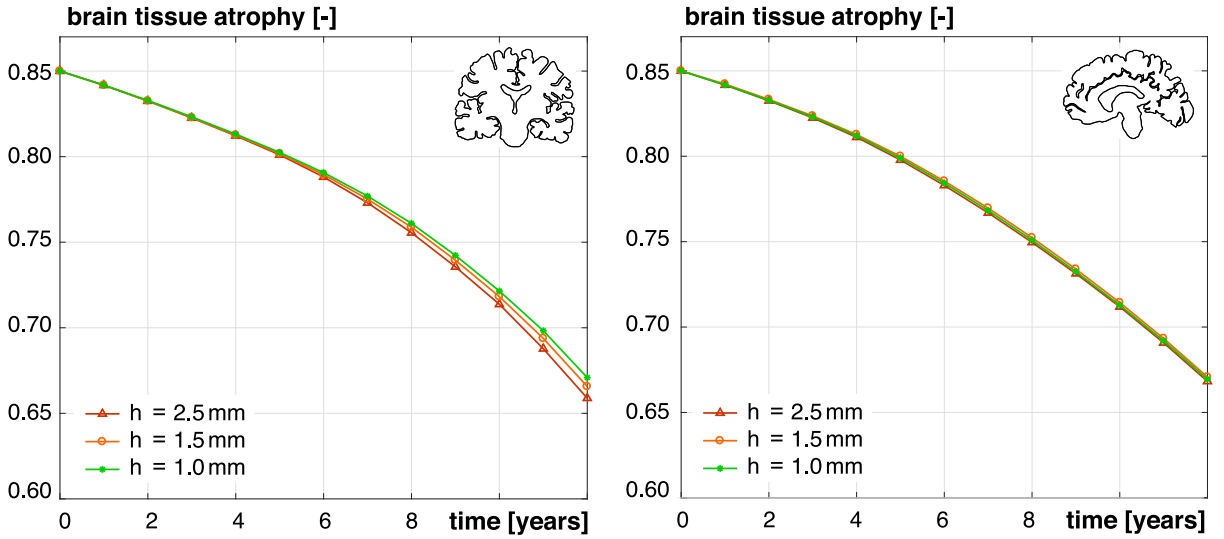

Fig. 5. Mesh convergence study for coronal (left) and sagittal (right) models. Brain tissue atrophy over time for baseline model parameters and three different mesh sizes, with colors indicating the respective average mesh size.

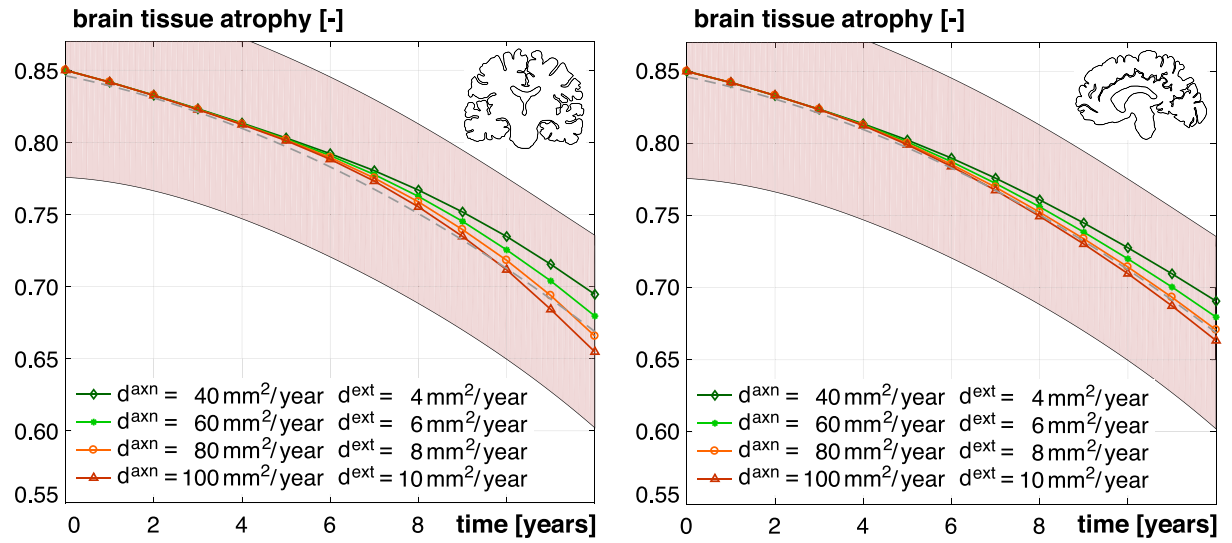

Fig. 6. Influence of the axonal transport and diffusion coefficients d^{axn} and d^{ext} on the evolution of atrophy over time. Results are plotted for coronal (left) and sagittal (right) models and four different values for d^{axn}, indicated by colors. The ratio between axonal transport and extracellular diffusion is fixed at $d^{\text{axn}} : d^{\text{ext}} = 10 : 1$. All other model parameters are fixed at their baseline values. The dashed gray curve and the light red 95% confidence interval summarize the cerebral atrophy data from twelve patients with early-onset Alzheimer's disease [17] from Fig. 1.

4.2. Sensitivity analysis

Figs. 6 to 9 summarize the results of our sensitivity analysis. Each figure shows the time in years on the horizontal axis and the dimensionless brain tissue atrophy with respect to total intracranial volume on the vertical axis. For each graph, we vary only one model parameter while keeping the remaining parameters fixed at their baseline values. These baseline values are $d^{\text{axn}} = 80\,\text{mm}^2/\text{year}$, $d^{\text{ext}} = 8\,\text{mm}^2/\text{year}$, $\alpha = 0.9/\text{year}$, $c^{\text{crit}} = 0.2$, $\dot{\vartheta}^{\text{gray}} = -4.5\%/\text{year}$ and $\dot{\vartheta}^{\text{white}} = -3.0\%/\text{year}$.

Fig. 6 shows the effect of axonal transport and extracellular diffusion on the evolution of cerebral atrophy. We model the tissue response with four different sets of axonal transport coefficients, $d^{\text{axn}} = 40\,\text{mm}^2/\text{year}$ (dark green curve), $d^{\text{axn}} = 60\,\text{mm}^2/\text{year}$ (light green curve), $d^{\text{axn}} = 80\,\text{mm}^2/\text{year}$ (orange curve), and $d^{\text{axn}} = 100\,\text{mm}^2/\text{year}$ (red curve). We adjust the extracellular diffusion coefficient accordingly to keep the ratio $d^{\text{axn}} : d^{\text{ext}} = 10 : 1$ constant. Varying the transport coefficients affects the overall slope of the atrophy curve after the onset of disease-induced atrophy. Lower coefficients result in an increased delay between the simulated onset of disease and visible consequences in the atrophy curve. The time at which the curves become linear again, after deviating from the healthy brain atrophy curve, marks the point in time at which the whole brain is saturated with misfolded protein. This event occurs earlier with larger transport and diffusion coefficients. Although both the natural atrophy rate and the misfolding induced atrophy rate are constant, the brain tissue atrophy displays a markedly nonlinear regime. This nonlinearity, after the onset of misfolding-induced atrophy and before the saturation of misfolded protein, reflects the heterogeneity of progressive spreading of misfolded protein across the brain. After complete saturation, all regions shrink at the same rate, resulting in a constant atrophy rate.

Fig. 7 summarizes the effect of the production of misfolded protein on the evolution of cerebral atrophy. We vary the production $\alpha = k_{12}\,k_0/k_1 - \tilde{k}_1$ between $\alpha = 0.7/\text{year}$ (dark green curve), $\alpha = 0.9/\text{year}$ (light green curve), and $\alpha = 1.1/\text{year}$ (orange curve), and keep the other parameters at their baseline values. We recall that an increase in the misfolded protein production can result from an increase in the conversion rate from healthy to misfolded protein k_{12}, an increase in the equilibrium concentration of healthy protein $p_0 = k_0/k_1$, or a decrease in the clearance of misfolded protein $\tilde{k}_1$. Modifying the production has a similar effect as modifying the axonal transport d^{axn}. The graphs illustrate that relatively high values for α are necessary to obtain an initial slope that matches the literature data, here shown as a dashed gray curve. However, high values for α also result in earlier saturation and earlier transformation of the curve from nonlinear to linear.

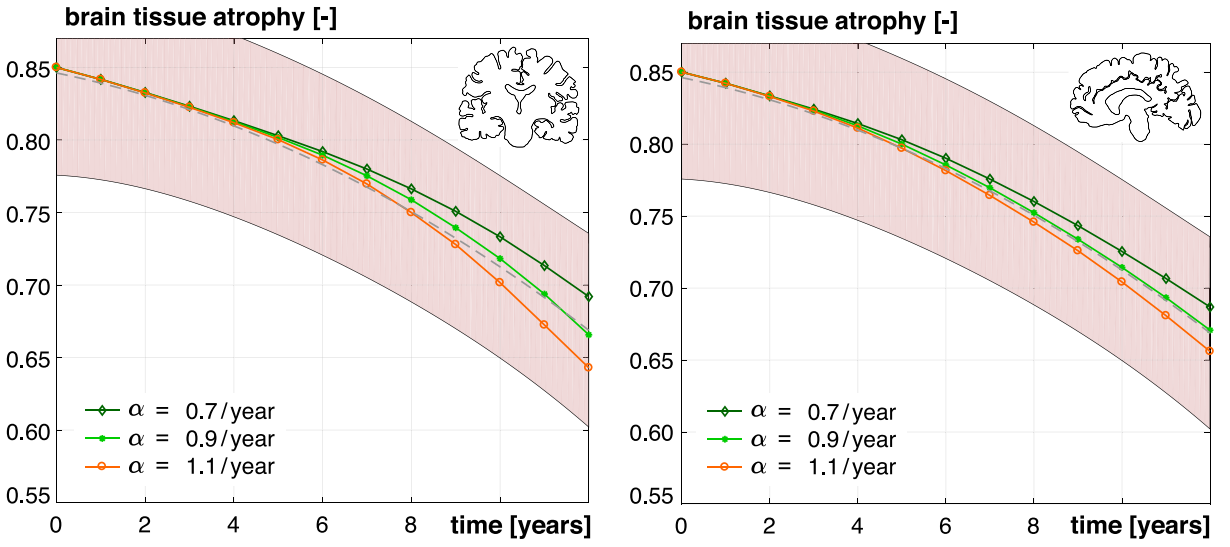

Fig. 7. Influence of the production of misfolded protein α on the evolution of atrophy over time. Results are plotted for coronal (left) and sagittal (right) slices and three different values for α, indicated by colors. All other model parameters are fixed at their baseline values. The dashed gray curve and the light red 95% confidence interval summarize the cerebral atrophy data from twelve patients with early-onset Alzheimer's disease [17] from Fig. 1.

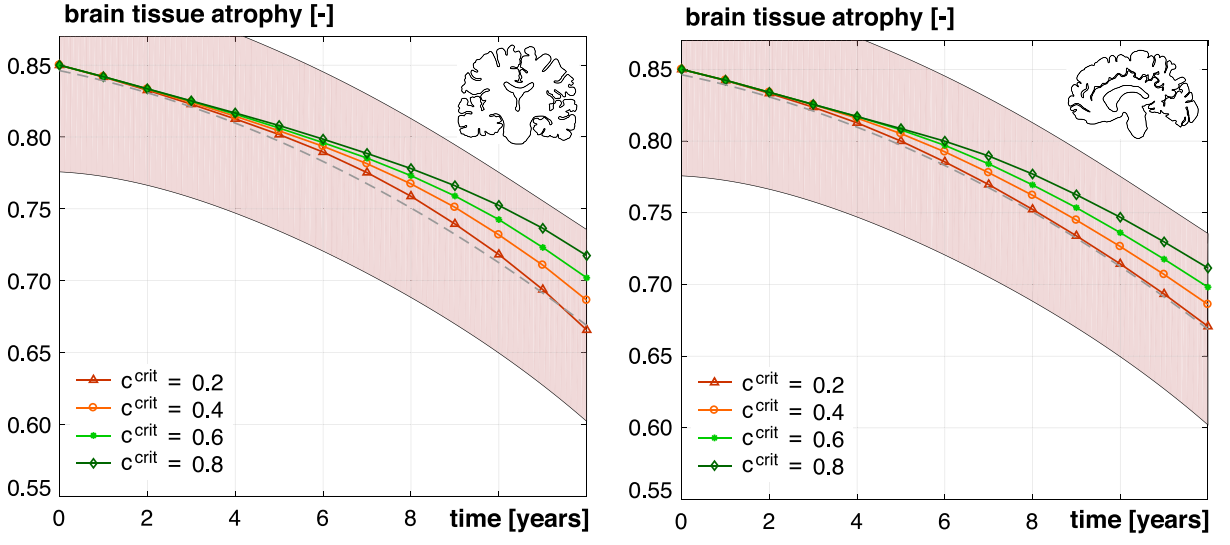

Fig. 8. Influence of the critical concentration c^{crit} on the evolution of atrophy over time. Results are plotted for coronal (left) and sagittal (right) slices and four different values for c_{crit}, indicated by colors. All other model parameters are fixed at their baseline values. The dashed gray curve and the light red 95% confidence interval summarize the cerebral atrophy data from twelve patients with early-onset Alzheimer's disease [17] from Fig. 1.

Fig. 8 shows the effect of the critical concentration on the evolution of cerebral atrophy. We vary the critical concentration between $c^{\text{crit}} = 0.2$ (red curve), $c^{\text{crit}} = 0.4$ (orange curve), $c^{\text{crit}} = 0.6$ (light green curve), and $c^{\text{crit}} = 0.8$ (dark green curve) and keep the other parameters at their baseline values. Increasing the value of the critical concentration c^{crit} shifts the onset of visible disease-induced atrophy to later points in time by increasing the tissue's tolerance to misfolded protein accumulation. While changing the critical concentration modulates the timing at which atrophy occurs, it does not affect the slope of the atrophy curves themselves.

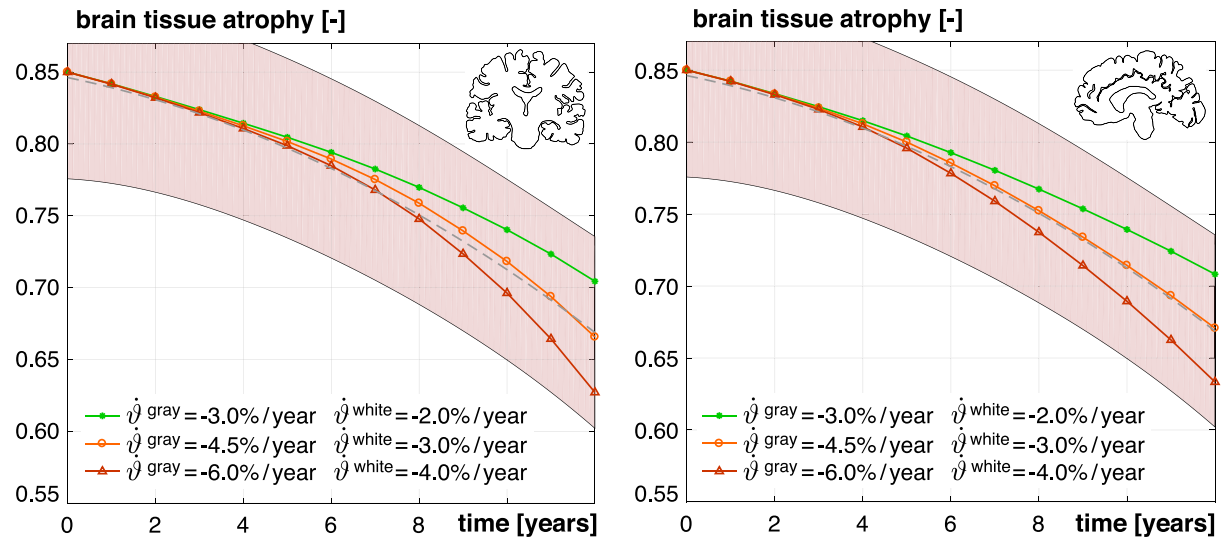

Fig. 9. Influence of the atrophy rates $\dot{\vartheta}^{\text{gray}}$ and $\dot{\vartheta}^{\text{white}}$ on the evolution of atrophy over time. Results are plotted for coronal (left) and sagittal (right) slices and three different atrophy rates, indicated by colors. All other model parameters are fixed at their baseline values. The dashed gray curve and the light red 95% confidence interval summarize the cerebral atrophy data from twelve patients with early-onset Alzheimer's disease [17] from Fig. 1.

Fig. 9 reveals the influence of the atrophy rates in gray and white matter $\dot{\vartheta}^{\text{gray}}$ and $\dot{\vartheta}^{\text{white}}$. We vary the gray matter atrophy rate between $\dot{\vartheta}^{\text{gray}} = -3.0\%$/year (green curve), $\dot{\vartheta}^{\text{gray}} = -4.5\%$/year (orange curve), and $\dot{\vartheta}^{\text{gray}} = -6.0\%$/year (red curve), and adjust the white matter atrophy rate accordingly to keep the ratio $\dot{\vartheta}^{\text{gray}} : \dot{\vartheta}^{\text{white}} = 3 : 2$ constant. Increasing the atrophy rate increases the slopes of the nonlinear segment of the graph and of the linear segment after the misfolded protein concentration has saturated. The atrophy rate is the parameter that most directly influences the brain tissue loss and most strongly modulates the shape of the atrophy curve.

4.3. Spatio-temporal evolution of protein spreading and tissue atrophy

Fig. 10 summarizes the simulations with the baseline parameters $d^{\text{axn}} = 80$ mm^2/year, $d^{\text{ext}} = 8$ mm^2/year, $\alpha = 0.9$/year, $c^{\text{crit}} = 0.2$, $\dot{\vartheta}^{\text{gray}} = -4.5\%$/year and $\dot{\vartheta}^{\text{white}} = -3.0\%$/year. For both the coronal and sagittal model, our simulated atrophy curves agree well with the clinically recorded atrophy curves [19]. Figs. 11 and 12 illustrate the spatio-temporal evolution of the misfolded protein concentration, the atrophy factor, and the von Mises stress in color-coded contour plots.

The top rows in Figs. 11 and 12 illustrate that at the beginning of the simulation, the misfolded protein concentration only increases locally around the seeding areas. Over time, the amount of misfolded protein in the seeding areas increases and gradually spreads along the axonal network throughout the brain. In the sagittal slice, the fiber orientation forces the protein to first spread into the frontal lobe, before moving around the ventricles into the occipital lobe. Misfolded proteins will only arrive in the central upper regions of the brain towards the end of the spreading process. Due to the different geometries and axonal network orientations in the coronal and sagittal models, the coronal slice saturates faster than the sagittal slice, even when using identical model parameters.

The middle rows in Figs. 11 and 12 show the local atrophy factors, or, in other words, the remaining tissue volume fraction in response to an increasing concentration of misfolded protein. Here, the color blue indicates tissue regions which still have their original volume, $J^{\text{a}} = \vartheta = 1$. Both the coronal and sagittal simulations reveal a pronounced atrophy in the gray matter tissue. Areas near the seeding region begin to atrophy first, once the misfolded protein concentration exceeds the critical concentration. As time progresses, gradually more and more regions atrophy. It becomes clear that even after large parts of the brain are saturated, $c = 1$, the atrophy values vary regionally, depending on how early volume loss was locally initiated.

The bottom rows in Figs. 11 and 12 illustrate the stress concentrations in vulnerable regions across the brain as a result of protein concentration gradients, regionally varying atrophy rates, and different stiffnesses in the gray

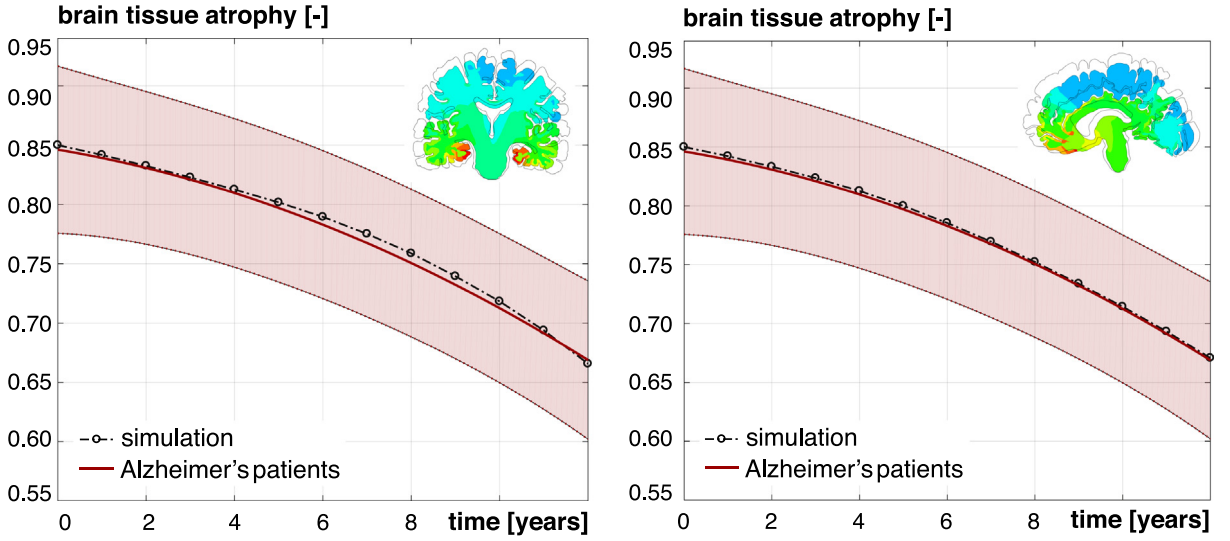

Fig. 10. Our simulations with the baseline parameters $d^{\text{axn}} = 80$ mm^2/year, $d^{\text{ext}} = 8$ mm^2/year, $\alpha = 0.9$/year, $c^{\text{crit}} = 0.2$, $\dot{\vartheta}^{\text{gray}} = -4.5\%$/year and $\dot{\vartheta}^{\text{white}} = -3.0\%$/year agree well with the clinically recorded atrophy, both for the coronal (left) and sagittal (right) models. The dashed black curve summarizes the results of the simulation; the solid red curve and the light red 95% confidence interval summarize the cerebral atrophy data from twelve patients with early-onset Alzheimer's disease [17] from Fig. 1.

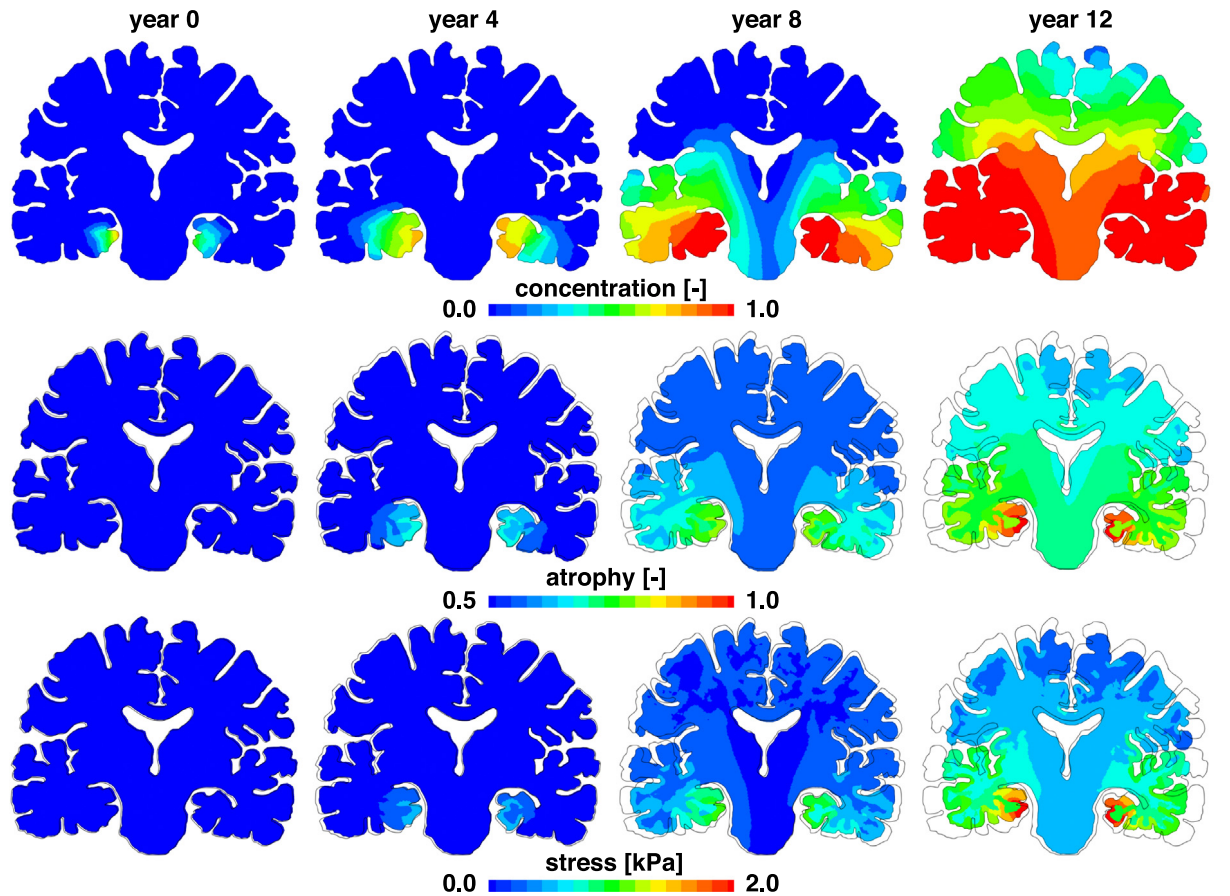

Fig. 11. Spatio-temporal evolution of the misfolded protein concentration c, the atrophy factor ϑ, and the von Mises stress σ at selected points in time, for a simulation with the coronal model, the medium mesh, and the baseline parameters.

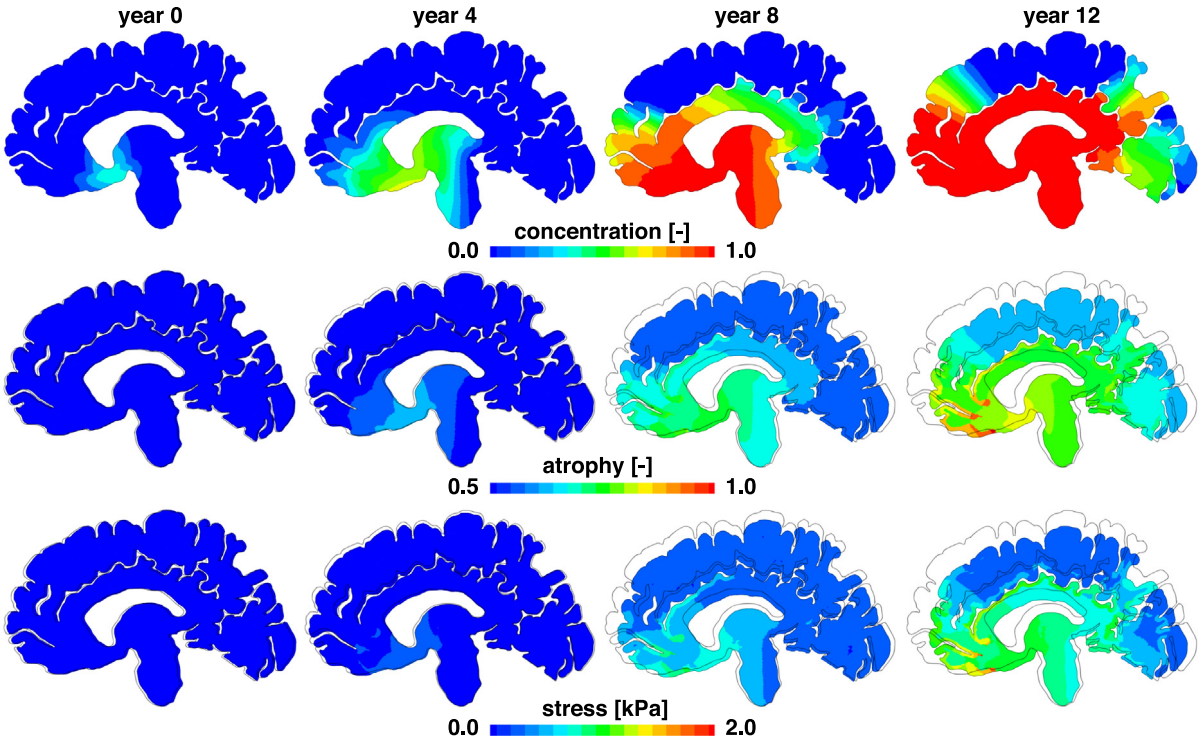

Fig. 12. Spatio-temporal evolution of the misfolded protein concentration c, the atrophy factor ϑ, and the von Mises stress σ at selected points in time, for a simulation with the sagittal model, the medium mesh, and the baseline parameters.

and white matter tissue. We assume that the cortex looses volume faster than the inner white matter. This induces tensional stresses in the gray matter resulting from the compatibility condition. The same principle leads to tensional stresses in the regions with elevated atrophy factors due to earlier initiation of tissue loss.

Fig. 13 illustrates the global concentration of misfolded proteins and the degree of brain tissue atrophy for both the coronal model and the sagittal model. The concentration curves reveal the characteristic sigmoid-like shape, which has been proposed in clinical biomarker models for neurodegeneration [3]. For the sagittal model, our simulation window of 15 years is too short to capture the saturation of the entire slice. This confirms once again that, due to different geometry and fiber orientations, misfolded proteins propagate slower across the sagittal slice than across the coronal slice. When comparing the evolutions of concentration and atrophy, we see the time delay between the onset of misfolding and the onset of disease-related atrophy, which we can modulate in our model though the critical concentration c^{crit}.

5. Discussion

Neurodegeneration and brain volume loss in Alzheimer's disease are associated with the spreading of misfolded tau protein across the brain. The objective of this study was to introduce a simple, physics-based computational model that connects the underlying biochemical process of protein spreading with the biomechanical process of tissue atrophy. We combined our recent model based on the classical Fisher–Kolmogorov equation with anisotropic diffusion [12] with a continuum model for anisotropic atrophy based on the brain's connectome. In this approach, protein spreading and tissue atrophy influence one another naturally through deformation-dependent diffusion and concentration-dependent shrinkage. Specifically, we proposed a novel constitutive model for concentration-dependent shrinkage in which the tissue atrophies at a natural rate that is accelerated in the presence of misfolded protein. Since the values of our model parameters are largely unknown, we probed their importance and effect on the simulation in a systematic parameter study. To compare the different results, we used the whole brain volume

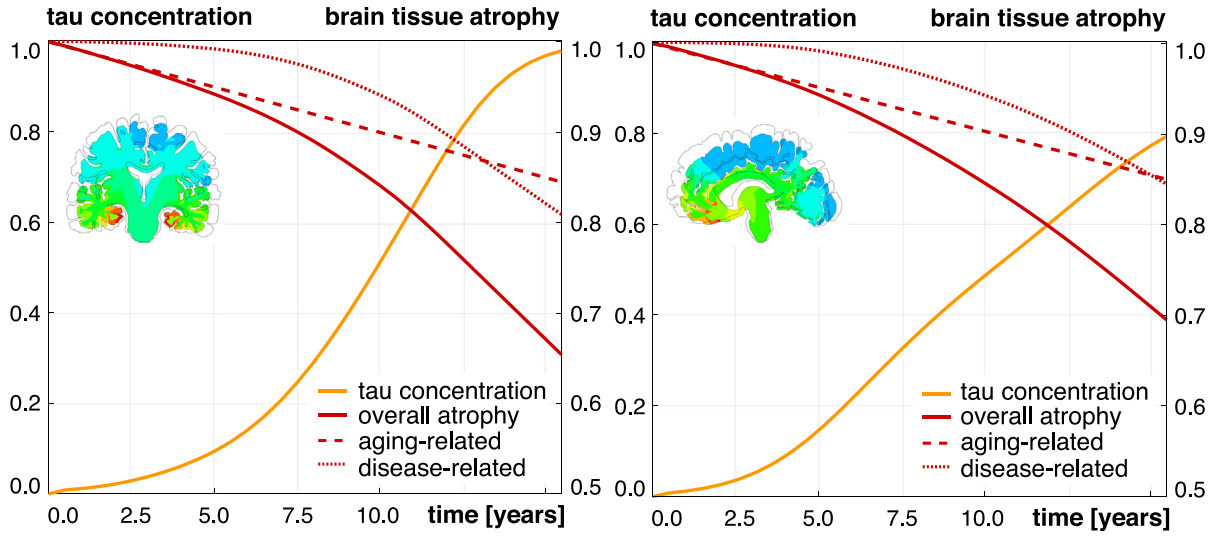

Fig. 13. Temporal evolution of global misfolded protein concentration and relative volume of the coronal model (left) and the sagittal model (right). The left vertical axes define the scale of the misfolded protein concentration (orange curves); the right vertical axes define the degree of brain tissue atrophy (red curves). The solid red curve illustrates the overall atrophy, the dashed and dotted curves show the individual contributions of aging-related and disease-related atrophy.

change over time as global metric for Alzheimer's disease progression. Our simulations confirmed our physical intuition and aligned well with clinical phenomena observed in early-onset Alzheimer's patients.

Extracellular diffusion, axonal transport, and growth control the timing of biochemical degeneration. In a previous study, we showed that spreading through extracellular diffusion d^{ext} and axonal transport d^{axn} has more influence on the three-dimensional protein propagation pattern than growth through the growth rate $\alpha = k_{12}\, k_0/k_1 - \tilde{k}_1$ [12]. All three parameters, extracellular diffusion d^{ext}, axonal transport d^{axn}, and growth α directly influence how fast misfolded proteins spread and how fast the local concentration saturates, which, in turn, indirectly affects how fast global atrophy progresses. From Figs. 6 and 7, we conclude that growth seems to affect the shape of the atrophy curve more than spreading, especially in the initial phase. Increasing the extracellular diffusion d^{ext} and axonal transport d^{axn} causes a faster spreading of protein per time step. This wider spreading implies that the local protein concentration decreases. In many regions, it will take longer for the local concentration to reach the critical concentration c^{crit} that triggers tissue atrophy and the atrophy curves remain close to the natural baseline atrophy at a natural slope of G_0. Increasing the growth rate α increases the amount of available misfolded protein. This leads to higher concentrations in all affected areas. The local concentration exceeds the critical concentration earlier in more regions. At the same time, an increased growth rate indirectly increases the spreading through the concentration gradient $\nabla_{\boldsymbol{x}} c$. In combination, this leads to steeper atrophy curves with slopes up to $G_0 + G_c$. A natural next step to improve our model would be to relate the parameters of extracellular diffusion, axonal transport, and growth to the underlying kinetics of prion-like update, replication, and release [33]. In combination with advanced kinetic modeling of prion-like replication, this would provide a more mechanistic interpretation of our model parameters [34]. We could refine the molecular model of protein misfolding even further by accounting for the misfolding and accumulation of amyloid-β [35]. In fact, it has been suggested that amyloid-β aggregation might be a trigger for the subsequent accumulation of misfolded tau protein [36]. To better capture the earliest events in the cascade of neurodegeneration in our simulation, we could include the amyloid-β concentration as a field of unknowns and simulate how amyloid-β precedes and influences the spreading of misfolded tau protein [8].

The critical concentration is a switch between biochemical and biomechanical degeneration. The critical concentration c^{crit} controls the sensitivity of the tissue with respect to the misfolded protein concentration. In that sense, it is the most important parameter that modulates the interplay between protein misfolding and cell death. Through the Heaviside function $\mathcal{H}(c - c^{\text{crit}})$, it effectively increases the natural baseline atrophy rate from $\dot{\vartheta} = G_0$ to $\dot{\vartheta} = G_0 + G_c$. In Fig. 8, we can observe this effect as a temporal shift between the accumulation of

misfolded protein and the onset of atrophy. An important future direction is the acquisition of quantitative knowledge about the relation between the two time scales of misfolded tau protein progression on the one hand and atrophy propagation on the other hand [35]. Since the biochemical processes of neurodegeneration precede the clinical diagnosis in Alzheimer's disease patients often by one or two decades this is a challenging task and most reported findings are hypothetical or qualitative at best [3,37]. Despite the lack of quantitative information, our model can easily account for varying temporal offsets between the protein spreading and tissue atrophy problems by adjusting equation (18), either by simply varying the critical concentration c^{crit} or by replacing the atrophy acceleration $\gamma(c)$. To date, it is unknown how much protein misfolding is too much protein misfolding for the cell to survive. From a modeling perspective, answering this question has important implications on the nature of coupling between biochemical and biomechanical degeneration. If the temporal shift between protein misfolding and tissue atrophy is large enough, the two problems naturally decouple and we can solve for protein misfolding first, store the time t^{crit} at which each integration point reaches the critical concentration c^{crit}, and then solve for tissue atrophy. Here we selected a value of $c^{\text{crit}} = 0.2$ as baseline value for our simulations. Once future experimental investigations reveal more quantitative information, we can easily change and adjust this value, or even change the amplification function, $\gamma = G_c/G_0\,\mathcal{H}(c - c^{\text{crit}})$, entirely. For example, instead of using the concentration only *implicitly* as a switch in the Heaviside function $\mathcal{H}(c - c^{\text{crit}})$, we could scale atrophy acceleration *explicitly* with the concentration itself, $\gamma = G_c/G_0\,c$. The inherent modularity of our model, especially with a view towards the biochemical and biomechanical coupling, will easily allow us to adjust the model to potential future findings, which could potentially emerge from positron emission tomography imaging of patients with familial or sporadic Alzheimer's disease.

The interplay of natural atrophy and misfolding-induced atrophy modulates biomechanical degeneration. The extracellular diffusion, axonal transport, and growth govern the timing of protein spreading whereas the critical concentration governs the time delay between the biomarkers of protein misfolding and tissue atrophy. In contrast, the tissue atrophy rates $\dot{\vartheta}^{\text{gray}} = G_0 + G_c^{\text{gray}}$ and $\dot{\vartheta}^{\text{white}} = G_0 + G_c^{\text{white}}$ only affect the biomechanical side of the problem. Varying these rates only affects the speed by which each affected element shrinks, but not the size of the activated domain. Changing their ratio $G_c^{\text{gray}} : G_c^{\text{white}}$, however, can generate different shrinkage patterns as we have previously shown [23]. Interestingly, we achieve a good fit for both, the coronal and the sagittal model, with identical model parameters in Fig. 9. This suggests that our atrophy model for neurodegeneration (18), $\dot{\vartheta} = G_0 + G_c$, in which atrophy is a result of the natural baseline atrophy rate G_0 and the misfolding induced atrophy rate G_c is a reasonable first approximation. The simulated curve becomes linear too early compared to the clinically reported curve [19]. However, a numerical fitting addressing these disparities will only make sense with a three dimensional whole brain geometry. Only then, a quantitative comparison with the literature data, in which volume and not area change is evaluated, can be made.

The predicted spatio-temporal patterns of degeneration mimic staging in the neurodegenerative disorders. After our systematic sensitivity analysis, we conclude that an axonal transport of $d^{\text{axn}} = 80\ \text{mm}^2/\text{year}$, an extracellular diffusion of $d^{\text{ext}} = 8\ \text{mm}^2/\text{year}$, a growth rate of $\alpha = 0.9$, a critical concentration of $c^{\text{crit}} = 0.2$, and atrophy rates of $\dot{\vartheta}^{\text{gray}} = -4.5\%/\text{year}$ and $\dot{\vartheta}^{\text{white}} = -3.0\%/\text{year}$ provide reasonable predictions of protein spreading and tissue atrophy. Our protein propagation patterns in Figs. 11 and 13, top, agree well with the staging sequence inferred from postmortem analyses [4,7]. Similar to biochemical degeneration, biomechanical degeneration first develops in the hippocampal periphery and then spreads throughout the temporal lobes and into the frontal lobe [15]. The occipital lobe is affected next, while the central areas comprising motor and sensory cortex are mainly spared. Not only our global atrophy curves in Fig. 10, but also the spatio-temporal patterns of atrophy in Figs. 11 and 13, middle, agree well with the observed timeline and sequence of degeneration. An important feature of our model is that it predicts regionally-varying degrees of atrophy across the brain, even after the entire brain geometry is saturated with misfolded protein. Modeling volume loss as a dynamic process that is initiated beyond a critical concentration and increases progressively in time naturally captures these observed characteristics [37]. Our model also nicely predicts a widening of the cerebral sulci, both in the coronal slice in Fig. 11 and in the sagittal slice in Fig. 13, a common feature of atrophy as evidenced through magnetic resonance imaging [38]. Another common observation associated with cerebral atrophy is the progressive increase in ventricular volumes, a feature that is not yet captured to full extent by our model. To better capture this effect, in the future, we will investigate the interplay of biochemical and fluid mechanical factors and include those effects in our model [39]. The stress distributions in Figs. 10 and 11, bottom, reveal elevated stresses due to regionally differential atrophy.

Elevated stresses occur in regions of pronounced stiffness and shrinkage gradients, primarily located at the interface between gray and white matter, in the depth of the cerebral sulci. These stress concentrations could potentially amplify protein misfolding or cause additional damage to the tissue [23]. A natural next step would be to simulate the interplay between protein spreading and tissue atrophy with a fully three-dimensional whole brain model. We have already made a first promising step in this direction and registered fiber orientations from diffusion tensor imaging on a three-dimensional finite element model of a healthy adult human brain [12]. While two-dimensional simulations provide excellent insight into the underlying phenomena, the role of the model parameters, and the nature of coupling between biochemistry and biomechanics [40], real three-dimensional simulations would provide a more realistic basis for the comparison with literature values on observed volume changes in time.

6. Conclusion

We proposed a multiphysics model that couples misfolded protein spreading and tissue atrophy to explore the spatio-temporal interplay of biochemical and biomechanical degeneration in Alzheimer's disease. Our predicted spatio-temporal patterns of protein spreading and tissue atrophy agree well with clinical observations inferred from in-vivo magnetic resonance imaging and post-mortem histopathology. Specifically, we observed high concentrations of misfolded protein and pronounced tissue atrophy in regions near the hippocampus. A critical link between biochemical and biomechanical degeneration is the rate of cerebral atrophy. This atrophy rate mimics both, natural aging-induced atrophy and accelerated misfolding-induced atrophy. Our simulations suggest that protein misfolding can accelerate natural atrophy between three- and five-fold. From a basic science point of view, computational modeling can improve our general understanding of the interplay between disease progression on the molecular and cellular scales on the one hand and atrophy progression on the tissue and organ scales on the other hand. From a translational point of view, once appropriately calibrated and validated, computational models of neurodegeneration could help improve diagnostic tools, advance early detection, and, ultimately, enable early interventions to delay the onset of cognitive decline in familial or sporadic Alzheimer's disease.

Acknowledgments

This work was supported by the Stanford Bio-X IIP seed grant "Molecular mechanisms of Chronic Traumatic Encephalopathy" and the National Science Foundation grant CMMI 1727268 "Understanding neurodegeneration across the scales".

References

[1] Alzheimer's Association, 2018. 2018 Alzheimer's disease facts and figures. Alzheimer's & Dementia 14, 367-429.
[2] L.E. Hebert, L.A. Beckett, P.A. Scherr, D.A. Evans, Annual incidence of Alzheimer disease in the United States projected to the years 2000 through 2050, Alzheimer Dis. Assoc. Disorders 15 (2001) 169–173.
[3] C.R. Jack, D.M. Holtzman, Biomarker modeling of Alzheimer's disease, Neuron 80 (2013) 1347–1358.
[4] H. Braak, E. Braak, Neuropathological staging of Alzheimer-related changes, Acta Neuropathologica 82 (1991) 239–259.
[5] H. Braak, E. Braak, Frequencey of stages of Alzheimer-related lesions in different age categories, Neurobiol. Aging 18 (1997) 351–357.
[6] D.R. Thal, U. Rub, M. Orantes, H. Braak, Phases of A beta-deposition in the human brain and its relevance for the development of AD, Neurology 58 (2002) 1791–1800.
[7] M. Jucker, L.C. Walker, Pathological protein seeding in alzheimer disease and other neurodegenerative disorders, Ann. Neurol. 70 (2011) 532–540.
[8] M. Jucker, L.C. Walker, Propagation and spread of pathogenic protein assemblies in neurodegenerative diseases, Nature Neurosci. 21 (2018) 1341–1349.
[9] M. Jucker, L.C. Walker, Self-propagation of pathogenic protein aggregates in neurodegenerative diseases, Nature 501 (2013) 45–51.
[10] S.B. Prusiner, Prions. Nobel lecture, Proc. Natl. Acad. Sci. 95 (1998) 13363–13383.
[11] J. Weickenmeier, E. Kuhl, A. Goriely, The multiphysics of prion-like diseases: progression and atrophy, Phys. Rev. Lett. 121 (2018) 158101.
[12] J. Weickenmeier, M. Jucker, A. Goriely, E. Kuhl, A physics-based model explains the prion-like features of neurodegeneration in Alzheimers disease, parkinsons disease, and amyotrophic lateral sclerosis, J. Mech. Phys. Solids 124 (2019) 264–281.
[13] G.B. Stokin, L.S. Goldstein, Axonal transport and Alzheimer's disease, Annu. Rev. Biochem. 75 (2006) 607–627.
[14] A. Raj, A. Kuceyeski, M. Weiner, A network diffusion model of disease progression in dementia, Neuron 73 (2012) 1204–1215.
[15] P.M. Thompson, K.M. Hayashi, G. De Zubicaray, A.L. Janke, S.E. Rose, J. Semple, D. Herman, M.S. Hong, S.S. Dittmer, D.M. Doddrell, A.W. Toga, Dynamics of gray matter loss in Alzheimer's disease, J. Neurosci. 23 (2003) 994–1005.
[16] N.C. Fox, W.R. Crum, R.I. Scahill, J.M. Stevens, J.C. Janssen, M.N. Rossor, Imaging of onset and progression of Alzheimer's disease with voxel-compression mapping of serial magnetic resonance images, Lancet 358 (2001) 201–205.

[17] D. Chan, J.C. Janssen, J.L. Whitwell, H.C. Watt, R. Jenkins, C. Frost, M.N. Rossor, N.C. Fox, Change in rates of cerebral atrophy over time in early-onset alzheimer's disease: longitudinal MRI study, Lancet 362 (2003) 1121–1122.
[18] B.H. Ridha, J. Barnes, J.W. Bartlett, A. Godbolt, T. Pepple, M.N. Rossor, N.C. Fox, Tracking atrophy progression in familial Alzheimer's disease: a serial MRI study, Lancet Neurol. 5 (2006) 828–834.
[19] J.L. Whitwell, W.R. Crum, H.C. Watt, N.C. Fox, Normalization of cerebral volumes by use of intracranial volume: implications for longitudinal quantitative MR imaging, Amer. J. Neuroradiol. 22 (2001) 1483–1489.
[20] O. Camara, M. Schweiger, R.I. Scahill, W.R. Crum, B.I. Sneller, J.A. Schnabel, G.R. Ridgway, D.M. Cash, D.L. Hill, N.C. Fox, Phenomenological model of diffuse global and regional atrophy using finite-element methods, IEEE Trans. Med. Imaging 25 (2006) 1417–1430.
[21] B. Karacali, C. Davatzikos, Simulation of tissue atrophy using a topology preserving transformation model, IEEE Trans. Med. Imaging 25 (2006) 649–652.
[22] A.D.C. Smith, W.R. Crum, D.L. Hill, N.A. Thacker, P.A. Bromiley, Biomechanical simulation of atrophy in MR images, in: Medical Imaging 2003: Image Processing (5032), 2003, pp. 481–491.
[23] T.C. Harris, R. de Rooij, E. Kuhl, The shrinking brain: Cerebral atrophy following traumatic brain injury, Ann. Biomed. Eng. (2018) http://dx.doi.org/10.1007/s10439-018-02148-2.
[24] R.A. Fisher, The wave of advance of advantageous genes, Ann. Eugenics 7 (1937) 355–369.
[25] A.N. Kolmogorov, I.G. Petrovsky, N.S. Piskunov, Investigation of the equation of diffusion combined with increasing of the substance and its application to a biology problem, Bull. Moscow State Univ. Ser. A Math. Mech. 1 (1937) 1–25.
[26] S. Budday, G. Sommer, C. Birkl, C. Langkammer, J. Haybaeck, J. Kohnert, M. Bauer, F. Paulsen, P. Steinmann, E. Kuhl, G.A. Holzapfel, Mechanical characterization of human brain tissue, Acta Biomater. 48 (2017) 319–340.
[27] Abaqus 6.14. Analysis User's Manual. SIMULIA. Dassault Systèmes. 2014.
[28] C. Geuzaine, J.F. Remacle, Gmsh: A 3-D finite element mesh generator with built-in pre- and post-processing facilities, Internat. J. Numer. Methods Engrg. 79 (2009) 1309–1331.
[29] L. Concha, D.W. Gross, C. Beaulieu, Diffusion tensor tractography of the limbic system, Amer. J. Neuroradiol. 26 (2005) 2267–2274.
[30] N. Soni, A. Mehrotra, S. Behari, S. Kumar, N. Gupta, Diffusion-Tensor Imaging and tractography application in pre-operative planning of intra-axial brain lesions, Cureus 9 (2017) e1739.
[31] Y. Wu, D. Sun, Y. Wang, Y. Wang, S. Ou, Segmentation of the cingulum bundle in the human brain: a new perspective based on DSI tractography and fiber dissection study, Front. Neuroanatomy 10 (84) (2016).
[32] J. Ahrens, B. Geveci, C. Law, Paraview: An end-user tool for large data visualization, in: The Visualization Handbook, Vol. 717, 2005.
[33] J. Masel, V.A.A. Jansen, M.A. Nowak, Quantifying the kinetic parameters of prion replication, Biophys. Chem. 77 (1999) 139–152.
[34] T. Pöschel, H.V. Brilliantov, C. Frömmel, Kinetics of prion growth, Biophys. J. 85 (2003) 3460–3474.
[35] C.R. Jack, D.S. Knopman, W.J. Jagust, L.M. Shaw, P.S. Aisen, M.W. Weiner, R.C. Petersen, J.Q. Trojanowski, Hypothetical model of dynamic biomarkers of the Alzheimer's pathological cascade, Lancet Neurol. 9 (2010) 119–128.
[36] J. Hardy, D.J. Selkoe, The amyloid hypothesis of alzheimer's disease: progress and problems on the road to therapeutics, Science 297 (2002) 353–356.
[37] H. Cho, J.Y. Choi, M.S. Hwang, Y.J. Kim, H.M. Lee, H.S. Lee, J.H. Lee, Y.H. Ryu, M.S. Lee, C.H. Lyoo, In vivo cortical spreading pattern of tau and amyloid in the Alzheimer disease spectrum, Ann. Neurol. 80 (2016) 247–258.
[38] S. Lehericy, M. Marjanska, L. Mesrob, M. Sarazin, S. Kinkingnehun, Magnetic resonance imaging of Alzheimers disease, Eur. Radiol. 17 (2007) 347–362.
[39] A. Goriely, M.G.D. Geers, G.A. Holzapfel, J. Jayamohan, A. Jerusalem, S. Sivaloganathan, W. Squier, J.A.W. van Dommelen, S. Waters, E. Kuhl, Mechanics of the brain: Perspectives, challenges, and opportunities, Biomech. Model. Mechanobiol. 14 (2015) 931–965.
[40] H. van den Bedem, E. Kuhl, Molecular mechanisms of chronic traumatic encephalopathy, Curr. Opin. Biomed. Eng. 1 (2017) 23–30.